DOMINANT TOUGHENING MECHANISMS IN BARIUM
ALUMINOSILICATE (BAS) GLASS-CERAMICS

By

JASON ALAN GRIGGS

ACKNOWLEDGMENTS

I would like to thank my wife, Amy, for enduring all of the lonely nights. I owe the timely completion of my graduate studies to her encouragement. Likewise, I would never have written this dissertation if it were not for my parents teaching me the value of an education and supporting my interest in the physical sciences.

I am also indebted to my mentors. Dr. Jack Mecholsky filled me with his passion for the subject of fracture mechanics and taught me the art of failure analysis. Dr. Ken Anusavice kept me from straying too far from clinical relevance. He coached my writing and presentation skills and prepared me for survival in the world of academic research.

TABLE OF CONTENTS

LIST OF TABLES

LIST OF FIGURES

Abstract of Dissertation Presented to the Graduate School
of the University of Florida in Partial Fulfillment of the
Requirements for the Degree of Doctor of Philosophy

DOMINANT TOUGHENING MECHANISMS IN BARIUM
ALUMINOSILICATE (BAS) GLASS-CERAMICS

By

Jason Alan Griggs

August, 1998

Chair: John J. Mecholsky, Jr.
Cochair: Kenneth J. Anusavice
Major Department: Materials Science and Engineering

The purpose of this study was to develop a barium aluminosilicate (BAS) glass-
ceramic with improved strength and fracture toughness by controlling the morphology of
the constituent phases through a series of thermal crystallization treatments. The specific
objectives of this study were as follows: 1) to determine which toughening mechanisms
are active in the BAS system, 2) to provide quantitative estimates of the relative
contributions of those mechanisms, and 3) to identify the processing conditions that
correspond to the glass-ceramic with the highest fracture toughness. The BAS system
was chosen for this study because of its potential applications in CAD-CAM production
of dental prostheses. It was concluded that stress transfer between the glass and crystal
phases and crack deflection are the only major sources of toughening in the BAS system.
Theoretical predictions for toughening associated with stress transfer and crack deflection

were sufficient to account for 100% of the increases observed. The flexural strength and fracture toughness of BAS glass-ceramics increased with increasing crystal growth time. The strength and fracture toughness increased from 63 ± 8 MPa and 0.89 ± 0.05 MPa·m$^{1/2}$, respectively, for BAS glass to 141 ± 8 MPa and 1.87 ± 0.07 MPa·m$^{1/2}$, respectively, for a glass-ceramic treated at 975°C for 256 h. Fracture toughness also increased with increasing mean crystal size. The addition of glass network modifiers resulted in thermal compatibility between the glass and crystal phases, preventing the weakening effect at large crystal sizes associated with spontaneous microcracking.

CHAPTER 1
PURPOSE

1.1 Process Rationale

The glass-ceramic method offers several advantages over ceramic powder processes. It is relatively easy to cast glass into complex and thin-walled shapes. Glass-ceramics can be produced near theoretical density with low processing shrinkage and without high-temperature drying and sintering operations. Furthermore, glass-ceramics are well suited for applications requiring specific optical properties because the translucency of a glass-ceramic can be controlled by varying the crystal size and volume fraction. A limitation of glass-ceramics currently used for dental applications is that they tend to have low fracture toughness values (0.7 to 2.0 MPa•m$^{1/2}$). To improve the structural reliability of these materials, it is necessary to understand how their constituent phases and microstructures interact to control their mechanical behavior.

1.2 Material Selection

The barium aluminosilicate (BAS) glass system was chosen for this study because glass compositions containing mica, a crystal phase with morphology and atomic structure similar to those of BAS crystals, have displayed excellent machinability and are potentially useful for CAD-CAM systems available in dentistry. Two mica-based glass-ceramics, Dicor® and Dicor MGC®, are commercially available as dental prosthetic

materials. This research was part of a project to produce a dental prosthetic material with greater strength, fracture toughness, and translucency than existing materials.

1.3 Research Objectives

The primary objective of this study was to identify the mechanisms responsible for increasing the fracture toughness of BAS glass-ceramics over that of the base glass and to estimate the relative contributions of those mechanisms. A secondary objective was to develop a process for the production of a BAS glass-ceramic with maximum fracture toughness. The specific aims of this study follow.

1.3.1 Specific Aim 1

Test the hypothesis that sources of toughening in the BAS system include mechanisms that are active in the frontal process zone, *e.g.*, crack deflection, as well as mechanisms that are active in the wake process zone, *e.g.*, crack bridging. This was accomplished by analyzing the dependence of fracture toughness on critical flaw size, *i.e.*, resistance-curve behavior, which usually indicates crack-particle interactions within the wake process zone. Also, a qualitative visual analysis of glass-ceramic fracture surfaces was used to search for evidence of crack bridging, frictional sliding, crack deflection, and flaw size limitation.

1.3.2 Specific Aim 2

Test the hypothesis that the dominant toughening mechanism associated with BAS glass-ceramics increases its contribution with increasing size of the reinforcing crystals, *e.g.*, crack deflection or crack bridging, and does not decrease its contribution

beyond a critical crystal size, *e.g.*, stress-induced microcracking. This goal was achieved by the use of stereological analyses to determine the size distribution of the crystal population in BAS glass-ceramics and by quantitative comparison of experimentally observed fracture toughness values with those predicted by theory for each toughening mechanism.

1.3.3 Specific Aim 3

Test the hypothesis that strength and fracture toughness can be optimized by selecting a microstructure with a maximum crystal size. Comparison of experimental strength and fracture toughness data revealed the crystal growth time which resulted in the highest strength and fracture toughness. A review of the results of previous strategies for processing BAS glass-ceramics suggested a strategy for production of the microstructure that corresponds to optimal mechanical properties.

CHAPTER 2
BACKGROUND

The following sections describe the methods used in fabrication of glass-ceramic materials and summarize the previous research that has been published on the synthesis and mechanical properties of barium aluminosilicate (BAS) glass-ceramics. Also included, is an in-depth review of several theories about the mechanisms responsible for increasing the strength and fracture toughness of glass-ceramics and glass-matrix composites in general above those of the base glass.

2.1 Glass-Ceramics

2.1.1 Processing of Glass-Ceramics

A glass-ceramic is a partly glass, partly crystalline solid prepared by the controlled crystallization of a glass. In theory, the glass-ceramic method consists of the following steps as shown in Figure 2.1: 1) melting ceramic powders or glass frits at high temperature to produce an amorphous liquid; 2) quenching the melt to a high viscosity before the ions have time to form an ordered crystalline lattice; 3) annealing the glass near the glass transition temperature to remove thermally induced stresses; 4) heating the glass to the nucleation temperature to add the ionic mobility necessary for the formation of crystal nuclei; and 5) heating the glass to the growth temperature to achieve the ionic diffusion necessary for growth of the nucleated crystals. In practice, the unique

4

properties of some parent glasses may allow elimination of some processing steps, *e.g.*, some phase-separating glasses such as BAS glass nucleate upon casting, allowing production of a fine microstructure without a crystal nucleation step. Alternatively, it may be beneficial to add a processing step, *e.g.*, photosensitive glasses produce heterogeneous nucleation sites when exposed to ultraviolet light.
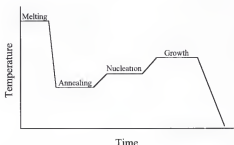
Figure 2.1. Diagram of the temperature-time cycle for the controlled crystallization of a glass-ceramic body.

Ideally, at the temperature that corresponds to the maximum rate of crystal nucleation, very little crystal growth occurs, and negligible crystal nucleation occurs at the temperature corresponding to the maximum crystal growth rate (Figure 2.2). The duration of the nucleation and growth treatments can be chosen to produce a crystal population with whatever spatial distribution and size distribution are desired. The optical and mechanical properties of the resulting glass-ceramic are a function of this microstructure. In large-scale production, however, isothermal heat treatments are rarely used, and the slow rates of heating and cooling that are employed allow less control over the reaction kinetics.
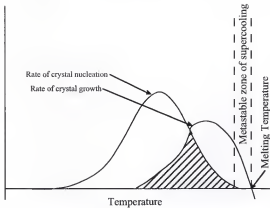
Figure 2.2. Diagram of the variation of crystal nucleation and growth rates with temperature.

Because the energy barrier to crystal nucleation is much lower at the external surfaces than in the bulk of the material, crystallization usually initiates on the external surfaces. This is followed by the crystals growing into the bulk and producing a population of large crystals with a wide distribution of sizes. Small crystals of uniform size are generally desirable for optimal mechanical properties, so nucleating agents such as P_2O_5 are often added to provide heterogeneous nucleation sites and to promote bulk crystallization.

The durations of nucleation and growth treatments necessary for crystallization depend on ionic mobility within the glass matrix. Ionic mobility is frequently increased through the addition of network modifiers, such as fluorides or alkali oxides, which decrease the number of bridging oxygens in the glass network. This allows the use of lower temperature furnaces or faster processing schedules.

2.1.2 BAS Glass-Ceramics

BAS glass-ceramics consist of a dispersion of BAS crystals surrounded by a continuous glass matrix. These glass-ceramics have attracted considerable interest as electronic and refractory materials because of their low dielectric constants and loss tangents and their high-temperature stability. BAS exists in three different crystalline polymorphs (Figure 2.3). The hexagonal form, hexacelsian ($BaAl_2Si_2O_8$), is stable from 1590°C to 1760°C but tends to be the first metastable product of synthesis outside this temperature range and persists below 1760°C. Hexacelsian crystals have a hexagonal plate morphology with a high aspect ratio. The crystal structure consists of di-tetrahedral sheets of alternating silica and alumina tetrahedra, which are weakly bonded by barium, calcium, or strontium ions (Figure 2.4). This weak bonding creates a basal (0001) cleavage plane similar to that responsible for the excellent machinability of mica-containing glass-ceramics (Chyung *et al.*, 1972). Below 300°C, hexacelsian crystals undergo a displacive transformation to the orthorhombic form with a 3% volumetric shrinkage. This may lead to microcracking and makes hexacelsian-containing ceramics unsuitable for thermal cycling applications. Previous research has focused mainly on accelerating the sluggish transformation to the thermodynamically stable monoclinic form, which is not susceptible to a displacive transformation and has a thermal expansion coefficient that is compatible with that of the stoichiometric glass phase.
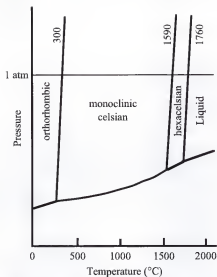
Figure 2.3. Pressure-temperature phase diagram for barium aluminosilicate according to Lin and Foster (1968).
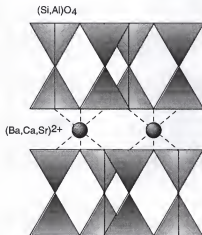
Figure 2.4. Diagram of the atomic structure of hexacelsian crystals according to Ito (1956).

Drummond and Bansal (1990) investigated BAS glass-ceramics as possible matrices in high-temperature structural composites. They nucleated glass frits of stoichiometric composition at either 850, 900, or 950°C for 1 h and then allowed crystal growth to occur at 1080, 1150, 1220, or 1290°C for 4 h. All combinations of thermal treatments resulted in the precipitation of mostly hexacelsian crystals with minor amounts of monoclinic celsian and residual glass. The glass-ceramic powders were cold pressed at 414 MPa and sintered at 1200 to 1500°C for 20 h. Three-point flexural strengths ranged from 62 MPa to 124 MPa with maximum strength corresponding to the lowest sintering temperature (Table 2.1). Glass-ceramic powders were also hot pressed at 1200 to 1400°C at a pressure of 24 MPa for 20 h. This resulted in a transformation to mostly monoclinic celsian crystals for all hot pressing temperatures.

Table 2.1. Properties of BAS glass-ceramics cold pressed at 414 MPa and sintered in air at various temperatures for 20 h according to Drummond and Bansal (1990).

Sintering Temperature (°C)	Pressing Additive (wt%)	Density (g/cm³)	Flexural Strength (MPa)
1200	0	3.06	124
1300	0	3.00	117
1400	0	2.87	62
1500	0	2.91	69
1200	5	3.05	103
1300	5	2.98	83
1400	5	2.86	83
1500	5	2.89	83

Talmy *et al.* (1992) investigated solid solutions of BAS and strontium aluminosilicate (SAS). They combined ceramic raw powders by substituting strontia for baria in concentrations of 0, 2, 5, 10, 25, 50, 75, 90, 95, and 100 mol% and seeding with 1

to 10 wt% of monoclinic celsian crystals. Specimens were cold pressed and sintered at 1050 to 1500°C for 5 h. Three-point flexural strengths ranged from 86 to 122 MPa with maximum strength at 25 mol% SAS (Figure 2.5). Conversion of BAS from the hexagonal form to the monoclinic form was augmented by both strontia substitution and monoclinic seeding.

Zaykoski and Talmy (1994) synthesized BAS ceramics by replacing aluminum with either 0, 50, or 100 mol% gallium and silicon with either 0, 50, or 100 mol% germanium. Glass frits were sintered at 1250 to 1550°C, and the strengths were determined through three-point flexure. Gallium and germanium substitutions decreased the sintering temperature necessary for conversion to monoclinic BAS; however, full substitution produced the paracelsian form of BAS. Flexural strengths ranged from 102 down to 64 MPa with maximum strength corresponding to the unsubstituted BAS ceramic (Table 2.2). This was attributed to the high volatility of germania that produced a large amount of surface porosity in the substituted specimens.

Zhou *et al.* (1997) prepared BAS glass-ceramics by hot pressing powders that were derived using the sol-gel method. They investigated stoichiometric BAS with additions of either 5 wt% monoclinic celsian seeds or 1, 3, or 5 wt% lithia. Specimens were hot pressed at 1100 to 1200°C at a pressure of 7 to 15 MPa for 0.5 h and fractured in a three-point flexural test. Lithia additions were effective in transforming hexacelsian crystals to monoclinic celsian crystals, and the addition of monoclinic seeds produced kinetics similar to those for 1 wt% lithia. The room temperature flexural strengths ranged from 140 down to 122 MPa with maximum strength corresponding to stoichiometric BAS

(Figure 2.6). Addition of 1 wt% lithia enhanced the high-temperature strength (148 MPa at 1200°C) but decreased the room-temperature strength.
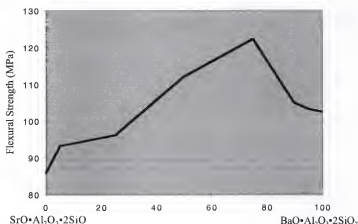
Figure 2.5. Flexural strength of ceramics in the system $SrO \cdot Al_2O_3 \cdot 2SiO_2$– $BaO \cdot Al_2O_3 \cdot 2SiO_2$ according to Talmy *et al.* (1992).

Table 2.2. Properties of ceramics of selected compositions in the $BaAl_2Si_2O_8$– $BaGa_2Ge_2O_8$ system according to Zaykoski and Talmy (1994).

Ga:Al	Ge:Si	Sintering Temperature (°C)	Flexural Strength (MPa)
0:2	0:2	1550	102
0:2	1:1	1500	76
0:2	2:0	1400	72
1:1	0:2	1450	87
1:1	1:1	1325	84
1:1	2:0	1275	76
2:0	0:2	1325	88
2:0	1:1	1250	68
2:0	2:0	1225	67
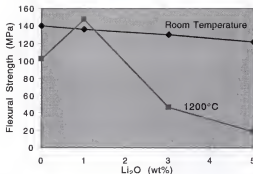
Figure 2.6. The effect of Li_2O content on the strength of celsian glass-ceramics according to Zhou *et al.* (1997).

2.2 Strength of Glass-Matrix Composites

To explain the improvement of strength in glass-ceramics or glass-matrix composites in general, researchers have focused on the following three mechanisms: 1) limiting the inherent flaw size in the matrix material by decreasing the mean free path between second-phase inclusions; 2) increasing the composite elastic modulus by adding high-modulus second-phase inclusions; and 3) increasing the energy necessary for crack extension through the interaction of cracks with second-phase inclusions.

2.2.1 Flaw Size Limitation

Griffith (1920) calculated the elastic energy stored in the vicinity of an elliptical flaw which is oriented with its major axis perpendicular to the direction of applied stress. Griffith showed that the elastic energy decreased as the flaw extended. He equated the decrease in stored energy with the energy needed to form two new fracture surfaces

during crack extension, yielding the following equation for the strength of a material, σ_0, in terms of the flaw size, a:

$$\sigma_0 = \left(\frac{4\gamma E}{\pi a}\right)^{1/2} \tag{2.1}$$

where γ is the surface energy and E is Young's modulus.

Hasselman and Fulrath (1966) hypothesized that a dispersion of hard inclusions would limit the size of Griffith flaws by decreasing the mean free path between crystals. They predicted that the mean free path of such a composite would fall within one of two regions (Figure 2.7). In Region I, the mean free path is larger than the mean flaw size. Only the largest flaw sizes are eliminated so that the composite strength can be described by the following expression:

$$\sigma = \frac{\sigma_0}{\left(1 - V_v\right)^{1/2}} \tag{2.2}$$

where σ_0 is the failure strength of the unreinforced glass, and V_v is the volume fraction of the dispersed phase.

For higher volume fractions or smaller particle sizes, the mean free path falls within Region II (Figure 2.7), and the sizes of all flaws are limited by the mean free path. This results in a greater dependence of composite strength on the volume fraction of the reinforcing phase, which Hasselman and Fulrath described by the following expression:

$$\sigma = \left[\frac{3\gamma E V_v}{\pi r\left(1 - V_v\right)}\right]^{1/2} \tag{2.3}$$

where r is the radius of the reinforcements. The experimental results of Hasselman and Fulrath, including Regions I and II, are shown in Figure 2.7.
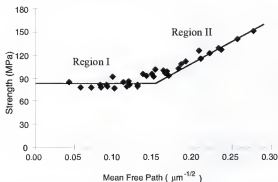
Figure 2.7. Plot of fracture strength versus reciprocal mean free path for glass specimens containing a dispersion of alumina particles according to Hasselman and Fulrath (1966).

Several subsequent studies on glass-ceramics and other glass-matrix composites (Bertolotti and Fulrath, 1967; Nivas and Fulrath, 1970; Stett and Fulrath, 1970; Hing and McMillan, 1973; Sproull and Rindone, 1973) support the theory of flaw size limitation; however, Borom (1977) re-examined these experimental data and concluded that an increase in the elastic modulus of the composite structure was more likely to be responsible for strengthening glass-matrix composites and that the inclusions may have actually increased the mean flaw size. Mecholsky and Freiman (1980) and Swearengen et al. (1978) confirmed that some reinforcing particles act as flaws which are larger than those of the intrinsic population.

<u>2.2.2 Stress Transfer</u>

Frey and Mackenzie (1967) proposed that a glass-matrix composite can be treated as a constant strain system. If the individual phases in a composite are considered well bonded at their interfaces, then the strains can be assumed to be equal, *i.e.,*

$$\varepsilon^d = \varepsilon^g = \varepsilon^c \qquad (2.4)$$

where the superscripts d, g, and c refer to the dispersed phase, the glass matrix, and the composite structure, respectively. Using Hooke's law, Equation (2.4) can be rewritten as

$$\frac{\sigma^d}{E^d} = \frac{\sigma^g}{E^g} = \frac{\sigma^c}{E^c} \qquad (2.5)$$

In other words, the constituent phases share the load in proportion to their elastic moduli with the more compliant matrix experiencing a lower stress than the rigid inclusions. Substitution of the rule of mixtures for composite modulus in equation (2.5) gives

$$\frac{\sigma_f^c}{\sigma_f^g} = \left[\left(1 - V_v \right) + \frac{E^d}{E^g} V_v \right] \qquad (2.6)$$

where the subscript f refers to the conditions at fracture. The strength of the composite is expected to increase with increasing volume fraction and elastic modulus of the dispersed phase.

Frey and Mackenzie (1967) tested this theory by adding alumina and zirconia dispersions to raise the elastic moduli of three glass compositions. They concluded that the glass-crystal composites acted like constant strain systems in that the strength was dependent on the elastic modulus. They also noted that the strengthening was due in part

to crack interaction with stress fields brought about by thermal expansion mismatch between the glass and crystalline phases.

Other researchers (Borom *et al.*, 1975; Swearengen *et al.*, 1978; Jessen *et al.*, 1986) subsequently confirmed the findings of Frey and Mackenzie. However, Jessen *et al.* and Swearengen *et al.* reported a greater increase in strength than could be attributed to stress transfer alone. Borom (1977) examined the existing literature and found that the data which had previously supported the flaw size limitation theory of Hasselman and Fulrath could also be explained in terms of stress transfer (Figure 2.8). He accounted for the difference between expected and observed strengths by proposing that the dispersed phase introduced flaws into the matrix in addition to increasing the elastic modulus of the composite. This explains why strengths lower than that of glass alone are observed for low volume fraction additions of a dispersed phase.
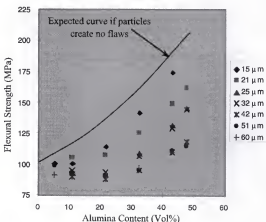
Figure 2.8. Flexural strength versus alumina content for various diameters of alumina reinforcements according to Borom (1977).

2.2.3 Crack-Particle Interaction

Another approach to increasing the reliability of glass-matrix composites is to impart sufficient fracture toughness so that the strength becomes insensitive to the size of flaws. This approach has the advantage that appreciable postprocessing damage can be tolerated. Also, fracture toughness provides a more objective measure of structural reliability than does strength, since fracture toughness is an intrinsic material property that is not dependent on the flaw distribution or specimen geometry. Numerous mechanisms have been proposed in which a growing crack interacts with particles of the reinforcing phase or the local stress fields associated with them to increase the fracture toughness of composites. These mechanisms are described in the following section.

2.3 Fracture Toughness of Glass-Matrix Composites

2.3.1 Crack Bowing

Lange (1970) proposed that when a crack front encounters inclusions, it is pinned in place and bows out between them, thereby increasing its overall length (Figure 2.9). Assuming that a crack front has a line energy per unit length, this bowing would increase the energy needed for crack propagation. Lange proposed that the increase in crack front length should be related to the distance between pinning inclusions and the curvature of the crack front just prior to crack extension. This hypothesis led to the following expression for fracture energy of the composite material:

$$\gamma = \gamma_a + \frac{T_\perp}{d} \tag{2.7}$$

where γ_0 is the fracture energy of the matrix material, T_c is the critical line energy per unit length of the crack front, and d is the distance between pinning inclusions. This expression is similar to those derived from the theory of Hasselman and Fulrath (Equations 2.2 and 2.3) in that both models incorporate the mean free path between inclusions.
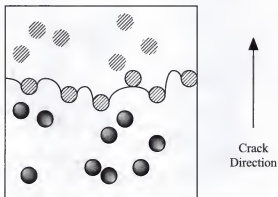
Figure 2.9. Diagram of the crack bowing mechanism proposed by Lange (1970). Propagating cracks are pinned at adjacent inclusions and bow out between them until increased local stress intensity enables the crack to break away from the pinning positions.

Lange (1971) tested his theory by adding dispersions of alumina to a glass and measuring the strength and fracture energy. The glass was formulated to minimize the difference in thermal expansion between the matrix and alumina, thereby ensuring negligible thermally induced stresses. Lange found that his model fit the experimental data well if he modified it to include the size of the reinforcing particles.

A basic assumption of Lange's crack bowing model was that the crack front would be semicircular in shape at the point when crack extension proceeded. Evans (1972) later showed that this was an extreme case, and he developed a model in which the crack front geometry was a function of the size and shape of impenetrable inclusions. Green *et al.* (1979) subsequently derived a model for the case of weak inclusions and pores, which predicts strength values higher than those observed for a glass-nickel system.

2.3.2 Crack Deflection

When there is a difference in thermal expansion between an inclusion and the surrounding matrix, the two phases contract at different rates upon cooling from high-temperature processing. This creates a residual thermally induced stress field that is locally associated with each inclusion. When the inclusion has a higher coefficient of thermal expansion than the matrix, the resulting stress field in the matrix adjacent to the inclusion consists of hoop compression and radial tension (Figure 2.10). Binns (1962), Stett and Fulrath (1970), and Khaund *et al.* (1977) observed that a propagating crack was deflected around the compressive stress field, thereby increasing the surface area of the resulting fracture surface and hence the fracture energy. The contribution to fracture toughness from an increased surface area mechanism is small; however, it was later recognized that an important difference exists between crack bowing, which produces a nonlinear crack front, and crack deflection, which produces a nonplanar crack. A reduction in stress intensity results when the propagating crack is forced out of its original plane of advance.

Faber and Evans (1983a) were the first to derive a quantitative relationship for crack deflection contributions to fracture toughness. They predicted that the size of the reinforcing particles would not be a determining factor, but that particle shape and volume fraction would be important. For low volume fractions of the reinforcing phase, the crack alters its path by tilting out of plane. For high volume fractions, the proximity of the particles sometimes causes the crack to twist with both sides of the crack tilting in opposite directions. Twist-derived toughening dominates whenever it occurs so that higher volume fractions yield a greater degree of toughening. Crack deflection toughening is also sensitive to the aspect ratio of the reinforcing particles since larger aspect ratios result in higher fracture toughness, especially for plate-shaped inclusions (Figure 2.11).
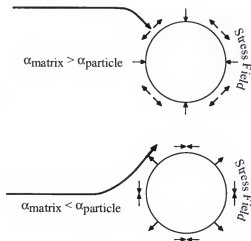
Figure 2.10. Diagram of the effect of thermal expansion mismatch between the matrix phase and the particulate phase on the path of a propagating crack.

Faber and Evans confirmed their predictions for spherical and rod-shaped particles by measuring the fracture toughness of lithium aluminosilicate glass-ceramics and hot-pressed silicon nitride (1983b). Sakai (1991) has criticized the *a priori* assumption of crack deflection made by Faber and Evans without consideration of the strength of the reinforcing particles or their bonding to the matrix material. Sakai points out that there have never been experimentally reported toughness increases as high as the theoretical predictions. More recently, Pezzotti (1993) conducted stereological simulations on dispersions of plate-shaped reinforcements. Pezzotti refuted the analysis of Faber and Evans on the basis that the spatial distribution function they employ considers only the distance of the nearest-neighboring particle in calculation of the mean free path between reinforcements. Pezzotti predicts that platelets can provide a maximum of 40% increase in fracture toughness over that of the matrix alone.
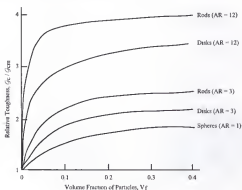
Figure 2.11. Normalized toughness predictions for a crack deflection mechanism for spherical, rod-shaped, and disk-shaped reinforcing particles with aspect ratios of 1, 3, and 12 according to Faber and Evans (1983a).

2.3.3 Crack Bridging

As a crack propagates through a composite material, strong reinforcing particles may be left unfractured in its wake. For large cracks, a growing number of intact reinforcements bridge the crack providing a closing force. The resistance to fracture increases with increasing crack size, leading to the classic resistance-curve (R-curve) behavior which is characteristic of toughening mechanisms that operate in the wake of the crack-tip process zone (Figure 2.12). Knehans and Steinbrech (1982) demonstrated the importance of the reinforcements by inducing stable crack propagation in polycrystalline alumina and then removing the material from the crack wake. Upon reloading, they observed a decrease in fracture toughness to that corresponding to small cracks.
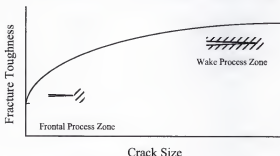
Figure 2.12. Diagram of the R-curve behavior of a brittle material subject to wake process-zone toughening mechanisms.

Crack bridging is usually associated with ductile reinforcements that can dissipate energy through plastic deformation instead of fracture; however, brittle reinforcements with sufficient size and strength can bridge a crack and dissipate energy through debonding from the matrix and frictional sliding (Figure 2.13). Long particles with high

strength and elastic modulus, as well as, a low interfacial strength are desirable to maximize the contribution of debonding and pullout mechanisms (Evans and McMeeking, 1986; Budiansky *et al.*, 1988). Although several theoretical models have been developed, experimental evidence of brittle crack bridging has been limited to fiber-reinforced composites and coarse-grained alumina (Knehans and Steinbrech, 1982; Swanson *et al.*, 1987).
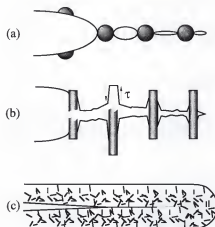
Figure 2.13. Diagram of possible toughening mechanisms operating in the wake process zone: (a) crack bridging, (b) debonding and pullout, and (c) stress-induced microcracking.

2.3.4 Microcracking

Binns (1962) and Davidge and Green (1968) found that thermally induced stresses beyond a critical magnitude can generate a dispersion of cracks on the same size scale as the microstructure. This spontaneous microcracking was observed to lower the strength and elastic modulus of glass-matrix composites. When the glass has a lower coefficient of

thermal expansion than the reinforcing phase, microcracks form around the circumference of the particles as they pull away from the matrix. When the glass has a higher coefficient of thermal expansion than the reinforcing phase, microcracks propagate radially from the particles. Coalescence of radial microcracks causes a greater degradation of the mechanical properties. A similar phenomenon can also develop from thermal anisotropy within the reinforcing phase (Evans, 1978).

At subcritical magnitudes of thermally induced stress, microcracks can increase fracture toughness. As the crack tip advances near a pre-stressed inclusion, the stress field associated with the crack tip is superimposed on the one associated with the inclusion. If the combined stress surpasses a critical level, then a stress-induced microcrack is developed. The development of microcracks during stable crack propagation was detected acoustically by Evans et al. (1974) and explained by Hoagland et al. (1975), Evans (1976), and Green (1981) who also predicted the shape and size of the microcracked zone. Hoagland and Embury (1980) have verified the predicted shape of the microcracked zone using a discrete computer model. Evans and Faber (1981; 1984) later derived quantitative predictions for microcrack toughening by the following two mechanisms: 1) dissipation of the stored elastic energy and 2) creation of a low-modulus zone around the crack tip which shields it from applied loading. They showed that particle size, interfacial strength, and particle size distribution are the most important factors affecting microcrack toughening.

The potential for microcrack toughening seems limited because Evans and Faber predict that a narrow particle size distribution with a mean particle size within 95% of

the critical size for spontaneous microcracking is necessary to achieve a significant effect, and particle sizes larger than this result in a lower composite fracture toughness than that for the glass matrix alone (Figure 2.14). Rice and Freiman (1981) also predict a strong dependence of microcrack toughening on particle size. Because microcracks continue to shield the crack in the wake process zone, this mechanism is expected to result in R-curve behavior similar to that produced by crack bridging (Figure 2.12).

Mean Crystal Size
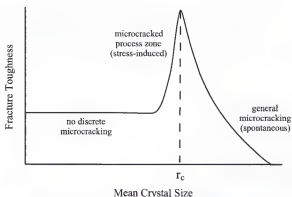
Figure 2.14. Diagram of the effect of particle size on the fracture toughness of a material susceptible to microcracking. Little toughening is observed until the mean particle size is close to a critical size, r_c. Fracture toughness decreases for larger particles.

2.3.5 Transformation Toughening

Transformation toughening has great potential as a toughening mechanism. It is not covered in detail here because it requires volumetric expansion from a metastable phase, such as partially-stabilized zirconia. The hexacelsian phase is the only metastable

phase found in the BAS system, and it undergoes a 3% volumetric shrinkage during the transformation to orthorhombic celsian.

3.1 Materials Fabrication

3.1.1 Glass Composition

The BAS glass used in this study had the composition 31.9 wt% SiO_2, 20.1 wt% Al_2O_3, 22.0 wt% BaO, 8.43 wt% MgO, 2.97 wt% CaO, 8.23 wt% MgF_2, and 6.42 wt% P_2O_5. This is the composition used by Uno *et al.* (1991) in a study of high-strength mica-containing glass-ceramics. A 154 kg batch of frit was obtained from Specialty Glass Company (Oldsmar, FL). Compositional analyses of the glass were performed by Coors Ceramics Analytical Laboratory (Golden, CO) prior to melting and after casting. A summary of these analyses is presented in Table 3.1

Table 3.1. BAS glass compositions prior to melting and after casting.

Component	Composition (wt%)		
	As-Received Frit	Melt I	Melt II
SiO_2	31.9	32.1	31.9
Al_2O_3	20.1	20.4	20.1
BaO	22.0	21.9	22.0
MgO	8.43	9.07	9.73
MgF_2	8.23	7.00	9.73
P_2O_5	6.42	6.37	6.43
CaO	2.97	2.99	2.98

3.1.2 Glass Melting and Forming

The glass frit was melted in a covered 150 cm³ ZGS platinum crucible (Johnson Matthey, Seabrook, NH) in a refractory furnace (Deltech Model DT-31-RS-OS, Deltech Inc., Denver, CO) heated by electrically resistant molybdenum disilicide heating elements. The glass was melted at 1500°C for 1 h to prevent excessive fluoride volatilization. The glass melt was cast into a graphite mold (5.1 x 12.7 x 2.1 cm). After casting, the glass plates were immediately placed in an electric muffle furnace (Model F6020, Thermolyne Corporation, Dubuque, IA) at 600°C. The glass was annealed at 600°C for 1 h and furnace cooled to room temperature. Once cooled, the glass plates were sectioned into flexural test bars (24.0 x 3.5 x 6.0 mm) using a low-speed diamond-wheel saw (Model 650, South Bay Technology Inc., San Clemente, CA).

3.1.3 Thermal Crystallization Treatments

Crystallization of all glass specimens was carried out using one-stage isothermal treatments. BAS glass is pre-nucleated upon casting, and thus no further nucleation treatment was used. Crystal growth treatments of 0.5, 4, 32, and 256 h duration were performed at 975°C to minimize thermocouple deterioration. All thermal treatments were performed in an electric tube furnace (Model 54577, Lindberg Corporation, Watertown, WI). After crystal growth, glass-ceramic specimens were annealed at 600°C and furnace cooled to room temperature. A control group of glass specimens received no crystal growth treatment but were subjected to the same annealing treatment as the glass-ceramic specimens. Figure 3.1 illustrates the thermal history of the glass-ceramic specimens.
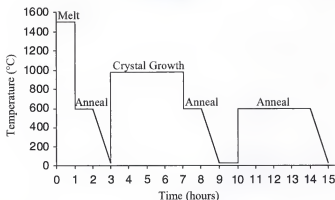
Figure 3.1. Thermal processing conditions for various stages of BAS glass-ceramic development.

3.2 Microstructural Analyses

3.2.1 Phase Identification

X-ray diffraction was employed to identify the crystal phases which precipitated from BAS glass over a range of temperatures. Glass specimens were heated from room temperature to 1050°C at 5°C/min. Beginning at 675°C, specimens were removed from the furnace and bench cooled at 15-min (75°C) intervals. Using a mortar and pestle, each specimen was ground and sieved to 325 mesh and then mixed with amyl acetate. The resulting slurry was mounted on a soda-lime glass slide and analyzed in an X-ray diffractometer (APD3720, Philips Electronic Instruments Inc., Mahwah, NJ) with a Cu K_α source. Scans were conducted at an intensity of 1000 counts/min over a 2θ range of 10° to 120° at 5°/min.

3.2.2 Crystal Morphology

The morphology of the crystalline phase was determined using the stereological methods of Fullman (1953) for analyzing a distribution of circular plates. Four specimens from each treatment group were sectioned at 90° and 45° angles to the length-wise direction using a low-speed diamond-wheel saw (Model 650, South Bay Technology Inc., San Clemente, CA). The sections were polished to a 1 μm finish using an alumina slurry and acid etched using 1% aqueous hydrofluoric acid for 10 s to reveal their microstructures. Two stereological fields were sampled from each section using an atomic force microscope (Nanoscope III Scanning Probe Microscope, Digital Instruments, Inc., Santa Barbara, CA) in the tapping mode. Fullman derived the following expressions for mean diameter ($\bar{d}$), thickness ($\bar{t}$), and aspect ratio ($\bar{a}$) of three-dimensional circular plates, respectively:

$$\bar{d} = \frac{\pi}{2\bar{E}}, \ \bar{t} = \frac{\pi\bar{G}}{4\bar{E}}, \text{ and } \bar{a} = \frac{3\pi^2\bar{F}}{32\bar{E}} \qquad (3.2, 3.3, 3.4)$$

where $\bar{E}$, $\bar{F}$, and $\bar{G}$ are the mean reciprocal length, width, and aspect ratio of the two-dimensional projections, respectively. Figure 2.2 illustrates the relationship between the two-dimensional geometry measured and the three-dimensional geometry of interest.

3.2.3 Glass Morphology

Standard stereological techniques were used to determine the crystalline volume fraction and the mean free path between crystals for each treatment group (Hilliard, 1968). Measurements of the two-dimensional projections of mica plates were made from the stereological fields used for the determination of crystal volume fraction. A 5 x 5 square grid was placed on each field, and point count measurements were made. The size

of the grid was chosen so that no more than one point fell within a given microstructural feature. The fraction of points falling within the crystalline phase was taken to equal the volume fraction of the crystalline phase. Figure 2.3 shows a typical point sampling.

The square grid used for determination of crystalline volume fraction was overlaid once again on the same stereological fields. A count was taken of the number of intersections between horizontal grid lines and crystal-glass interfaces per unit of grid line length. The mean free path between crystals, $\overline{\lambda}$, was calculated using the following expression:

$$\overline{\lambda} = \frac{1 - V_V}{0.5 N_{L\alpha\beta}} \tag{3.1}$$

where V_V is the crystalline volume fraction, and $N_{L\alpha\beta}$ is the number of lineal intercepts with crystal-glass interfaces per unit length.
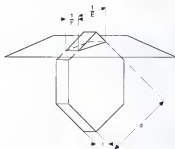
Figure 3.2. Diagram of a BAS crystal intersected by a stereological field. Measurements from the sections of many crystals are used to calculate parameters for the crystal population.
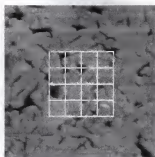
Figure 3.3. A point counting grid superimposed on a typical stereological field for determination of crystalline volume fraction and mean free path.

3.3 Physical Property Analyses

3.3.1 Density and Hardness

The densities of specimens were determined from measurements of mass and volume. One monolithic specimen from each treatment group was ultrasonically cleaned in ethanol. The dry weight of each specimen was determined using a precision balance (Model HL52, Mettler Instruments Corp., Hightstown, NJ). The volume of each specimen was measured using a helium micropycnometer (Model MPY-1, Quantachrome Corp., Syosset, NY).

A microhardness tester (Model MO Tukon Microhardness Tester, Wilson Instruments Inc., Binghamton, NY) with a Vickers diamond was used to measure the hardness of four specimens from each treatment group. Hardness specimens were flattened using a metal-bonded diamond abrasive disk. The surface to be indented was then polished to a 1 µm finish using an alumina slurry. The specimens were each

indented in four different locations under a 4.9 N load. The dimensions of the indentation diagonals were measured using an optical microscope with a filar eyepiece. The hardness values were calculated according to the following equation:

$$H = \frac{2P\sin\left(\frac{\theta}{2}\right)}{\bar{a}^2} \tag{3.7}$$

where P is the indentation load, θ is the angle between opposite diamond faces (136°), and $\bar{a}$ is the mean diagonal length of the indentation.

3.3.2 Elastic Constants

Elastic constants were calculated for eight specimens in each treatment group from the density and the velocity of sound through the material. The velocity of sound was measured using an ultrasonic pulse apparatus (Ultima 5100, Nuson Inc., Boalsburg, PA). Shear and longitudinal waves were generated using 5 MHz piezoelectric transducers (SC25-5 and WC25-5, Ultran Laboratories, Inc., Boalsburg, PA). The transducers were coupled to the specimens using honey and glycerin for shear and longitudinal waves, respectively. The electronic delay in the pulse apparatus was subtracted from the time-of-flight before calculating the velocity of sound. Poisson's ratios were calculated using the following expression:

$$\nu = \frac{1 - 2\left(\frac{v_s}{v_L}\right)^2}{2 - 2\left(\frac{v_s}{v_L}\right)^2} \tag{3.5}$$

where v_S is the shear velocity, and v_L is the longitudinal velocity. Young's modulus was calculated using the following expression:

$$E = \frac{\rho v_L^2 (1+v)(1-2v)}{1-v} \qquad (3.6)$$

where ρ is the density.

3.3.3 Thermal Expansion

Square plates were cut to produce a bar, 50 x 5 x 5 mm. One glass specimen from the control group was ground to a length of 50 ± 0.001 mm for thermal expansion measurement. The expansion was recorded using a single-pushrod dilatometer (Model EK2, The Edward Orton Jr. Ceramic Foundation, Columbus, OH). The specimen was heated from 25°C to 600°C at a rate of 3°C/min. The coefficient of thermal expansion was calculated from the cooling curve to eliminate the effects of residual thermally induced stress.

3.3.5 Flexural Strength

Four-point flexural bars were prepared by flattening all sides of a rectangular bar (24.0 x 3.5 x 6.0 mm) using a metal-bonded diamond abrasive disk. The side to be placed in tension was then polished to a 1 μm finish using an alumina slurry. All specimens were annealed at 600°C for 4 h following polishing to eliminate any compressive surface stresses. After annealing, the lengthwise edges on the tensile surfaces were beveled to prevent fracture initiation from the specimen edges. Eight specimens per treatment group were indented with a Vickers diamond at either of two indentation loads (4.9 or 9.8 N).

Each specimen was indented at three positions within the inner span length. Prior to indentation, a drop of silicone oil was placed on the tensile surface to inhibit moisture-assisted slow crack growth. All specimens were aged in ambient conditions for 24 h before fracture to allow stabilization of the controlled flaw size. The specimens were fractured using a Instron testing machine (Model 1125, Instron Corporation, Canton, MA) and a four-point bending apparatus (19.9 mm outer span, 6.4 mm inner span). Figure 3.4 illustrates the geometry of the loading apparatus. The specimens were loaded monotonically to fracture at a rate of 0.5 mm/min. The flexural strength was calculated using the following expression:

$$\sigma_f = \frac{3Px}{wt^2} \tag{3.8}$$

where P is the failure load, x is the distance between the inner and outer supports, w is the specimen width, and t is the specimen thickness.
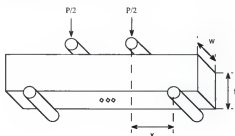
Figure 3.4. Diagram of the four-point bending apparatus used for the determination of flexural strength.

3.3.6 Fracture Toughness

Because fracture toughness was the material property of greatest interest in this study, three different methods were used to collect fracture toughness data. Each has its own advantages and disadvantages. Fractographic analysis involves direct examination of the fracture surface and measurement of the critical flaw from which fracture originated. Using this method, the indentation can be confirmed to be the site of fracture initiation. However, this method requires a great deal of experience, and many researchers have not acquired the skill necessary to make accurate measurements of critical flaw size (Quinn *et al.*, 1994).

The indentation-strength technique developed by Chantikul *et al.* (1981) does not require a measurement of the critical flaw size. Instead, a flaw size is assumed from the indentation load used to induce controlled flaws. This method eliminates some of the investigator-related error from data collection, but it is not accurate if environmentally-assisted slow crack growth occurs before fracture.

The modified indentation technique developed by Cook and Lawn (1983) involves inducing multiple controlled flaws and measuring the trace of the flaws which remain intact within the tensile surface after fracture. The boundaries of these intact flaws are usually easier to discern than those of the critical flaw. Because intact flaws are concealed within the tensile surface, only their widths and not their depths can be observed. These data may be misleading if the flaw is semi-elliptical instead of semi-circular in shape (Chan, 1996).

3.3.6.1 Fractographic analysis

Mecholsky *et al.* (1978) have established a protocol for determining fracture toughness via analysis of fracture surface features. The flexural strength specimens from Section 3.3.5 were used with the flaw size as determined through quantitative fractography to calculate fracture toughness.

The fractured pieces of each four-point flexural bar were ultrasonically cleaned in an aqueous detergent, followed by ethanol, and then sputter-coated with a gold-palladium alloy (Hummer II, Anatech Ltd., Alexandria, VA). The fracture surfaces were examined with an optical microscope, and the fracture surface features were measured using a filar eyepiece. The characteristic fracture surface features exhibited by glass-ceramics are shown in Figure 3.5.

After measuring the major and minor axes of the semi-elliptical flaws, the radii of the equivalent semi-circular flaws were calculated using the following relationship (Mecholsky *et al.*, 1977):

$$c = \left(ab\right)^{1/2} \tag{3.9}$$

where a and b are the depth and half-width of the flaw, respectively. The fracture toughness of each specimen was then calculated using the Griffith-Irwin equation:

$$K_{Ic} = Y\sigma_f c^{1/2} \tag{3.10}$$

where σ_f is the strength from Equation (3.7) and Y is a shape parameter that has been determined by Marshall *et al.* (1983) to be 1.65 for the residual stress associated with an indentation.
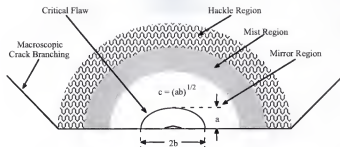
Figure 3.5. Diagram of the typical fracture surface features occurring in brittle materials. The regions are not drawn to scale.

3.3.6.2 Indentation-strength technique

The strength values already determined in Section 3.3.5 were used to determine fracture toughness using the following equation:

$$K_{Ic} = \eta_v^R \left(\frac{E}{H} \right)^{1/8} \left(\sigma_f P^{1/3} \right)^{3/4} \tag{3.11}$$

where η_v^R is a geometrical constant that Chantikul *et al.* (1981) determined to be 0.59 for a Vickers diamond, E is Young's modulus, H is the hardness, σ_f is the fracture stress from Equation (3.7), and P is the indentation load (4.9 or 9.8 N).

3.3.6.3 Modified indentation technique

Three controlled flaws were induced at different sites within the constant-stress, inner-span region of the four-point flexure specimens (Section 3.3.5). Because of slight inhomogeneities in the loading system, only one of the three flaws grew past critical size; however, the two remaining intact should have grown to nearly critical dimensions. The

half-width of the surface trace from the largest of the two intact flaws was measured for the crack size, c_m. Figure 3.6 shows the location of the intact flaw on a fracture specimen.

For glass-ceramic materials, the equation suggested by Cook and Lawn (1983) for calculation of fracture toughness yields values that do not agree with those determined using the fractographic and indentation-strength techniques (Chan, 1996; Hill, 1998). Instead, the Griffith-Irwin equation (3.9) with the modified crack size, c_m, was used to calculate fracture toughness. The flaw depth, a, of the intact semi-elliptical flaws was not visible from the surface trace, so the sizes of equivalent semi-circular flaws were estimated using Equation 3.8 with the mean ellipticity of the critical flaws, $\dfrac{a}{b} = 0.804$, as a conversion factor. The resulting equation for calculation of modified-indentation fracture toughness was as follows:

$$K_{IC} = Y\sigma_f \left(0.804\right)^{1/4} c_m^{1/2} \tag{3.12}$$

where σ_f is the strength from Equation (3.7), Y is a shape parameter that has been determined by Marshall et al. (1983) to be 1.65 for the residual stress associated with an indentation, and c_m is the half-width of the intact flaw.
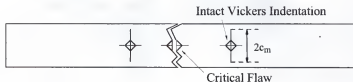
Figure 3.6. Diagram of the location of an intact controlled flaw on a fractured four-point flexure specimen. The flaws are not drawn to scale.

3.5 Finite Element Analyses

Finite element stress analyses were used to estimate the magnitude of the thermally induced stresses that develop adjacent to and between BAS crystals in the glass upon cooling from processing temperatures to ambient temperature. The ANSYS computer code (ANSYS 5.3, Swanson Analysis Systems, Inc., Houston, PA) was used to perform these analyses. Finite element meshes were generated using a two-dimensional, eight-node quadratic element (PLANE82). Models were developed for pairs of BAS crystals in a parallel edge-to-edge orientation. This geometry was examined using the mean crystal size and the mean free path between crystals determined for each treatment group in Sections 3.2.2 and 3.3.3. Figure 3.7 shows the model geometry and boundary conditions for the finite element simulations.
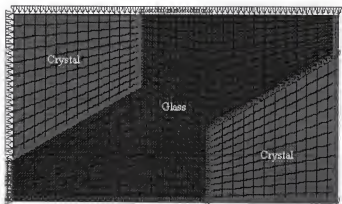
Figure 3.7. Finite element model for a pair of BAS crystals in a glass matrix. A zero-displacement boundary condition is applied at the top and left edges. A coincident node condition is applied at the bottom and right edges and along the crystal-glass interfaces.

The material properties used to model the glass phase were determined using the methods described in Sections 3.3.1 and 3.3.3. The following material properties were used for the glass phase: elastic modulus (E) = 94.1 GPa, Poisson's ratio (ν) = 0.284, and coefficient of thermal expansion (α) = 7.64 ppm/°C. The material properties used to model the crystal phase were calculated using the rule of mixtures and compared to values in the existing literature (Zhou *et al.*, 1997). The following material properties were used for the crystal phase: elastic modulus (E) = 110 GPa, Poisson's ratio (ν) = 0.257, and coefficient of thermal expansion (α) = 7.4 ppm/°C. Thermally induced stresses were estimated for cooling from the glass transition temperature, 600°C, to room temperature, 23°C. The source codes for these models are listed in Appendix A.

CHAPTER 4
RESULTS AND DISCUSSION

In the following sections, the data collected for microstructural and macroscopic properties of BAS glass and glass-ceramics are presented primarily in a graphical format (Sections 4.1 and 4.2). The mean properties ± 95% confidence intervals are compared for glass-ceramics with crystal growth treatments of 0.5, 4, 32, and 256 h in duration and contrasted with those of the base glass. The data for individual specimens are listed in Appendix B. The residual thermally induced stress distributions predicted by finite element analyses are presented (Section 4.3), and the roles of several mechanisms in strengthening and toughening of BAS glass-ceramics are discussed (Section 4.4). A quantitative estimate is made of the relative contribution of each mechanism to the observed strength and fracture toughness, and an optimal process is identified for producing BAS glass-ceramics from the selected glass composition. Future modifications for optimizing processing time and mechanical properties are suggested.

4.1 Microstructure

4.1.1 Phase Identification

Figure 4.1 shows the x-ray diffraction spectra for the crystalline phases that precipitated from the base glass at temperatures ranging from 675 to 1050°C at 75°C intervals. Comparison of these data with JC-PDS records revealed that only the

hexacelsian crystal phase was present. Uno *et al.* (1993) reported that a phlogopite crystal phase precipitated from base glass of the same composition when subjected to similar crystallization treatments. The atomic structures and physical properties of hexacelsian and phlogopite are similar and the crystal morphologies are identical.
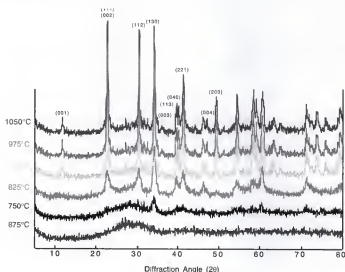
Figure 4.1. X-ray diffraction spectra for BAS glass-ceramics. Hexacelsian ($BaAl_2Si_2O_8$) is the only phase present. Peak intensity is a function of processing temperature.

4.1.2 Crystal Morphology

AFM micrographs of polished and etched BAS glass-ceramic microstructures for crystal growth treatments of 0.5, 4, 32, and 256 h in duration are shown in Figures 4.2 to 4.5, respectively. The crystals exhibited a hexagonal plate morphology in all specimens.

Figure 4.6 shows that no change in crystalline volume fraction occurred during crystal growth. Figure 4.7 shows the increase in mean crystal diameter and thickness with increasing crystal growth time. The crystalline volume fraction was observed to remain constant at 0.76 ± 0.02 over time. The mean crystal size increased over time, but the mean crystal aspect ratio, 3.81 ± 0.39, was independent of crystal size.

The crystallization of most glass-ceramic systems involves the transformation of an increasing amount of glass phase into ceramic phase over time. In BAS glass-ceramics, this process is completed within 30 min. Thereafter, a coarsening process occurs whereby the crystals smaller than a critical size dissolve into the matrix, and material from them is reprecipitated onto the larger crystals. Juma'a and Parker (1981) investigated calcium fluoride glass-ceramics in which crystal growth occurs through a coarsening process. They reported that, because the addition of fluoride increased ionic mobility within the glass, the growth of ceramic crystals was limited by the rate of the dissolution/precipitation reaction at the crystal surface and not by the diffusion rate of ions through the glass matrix. Consequently, the mean crystal size increased in direct proportion to the cube-root of the growth treatment duration, *i.e.*, eight times the processing time is necessary in order to double the mean crystal size. The growth kinetics of BAS glass-ceramics fit this model very well ($R^2 = 0.998$).
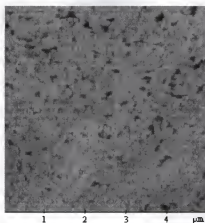
Figure 4.2. Atomic force micrograph of the microstructure of a BAS glass-ceramic produced by a crystal growth treatment at 975°C for 0.5 h.
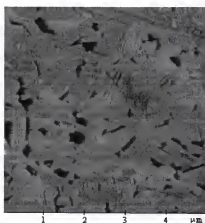
Figure 4.3. Atomic force micrograph of the microstructure of a BAS glass-ceramic produced by a crystal growth treatment at 975°C for 4 h.

Figure 4.4. Atomic force micrograph of the microstructure of a BAS glass-ceramic produced by a crystal growth treatment at 975°C for 32 h.

Figure 4.5. Atomic force micrograph of the microstructure of a BAS glass-ceramic produced by a crystal growth treatment at 975°C for 256 h.
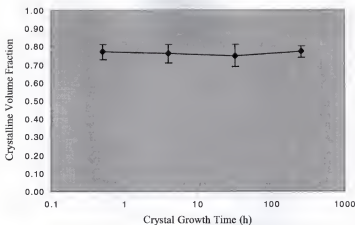
Figure 4.6. Effect of crystal growth time on the crystalline volume fraction of BAS glass-ceramics.
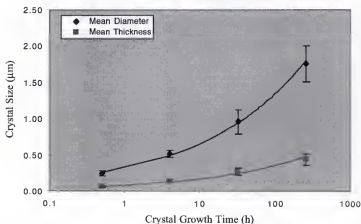
Figure 4.7. Effect of crystal growth time on the morphology of the crystalline phase in BAS glass-ceramics.

4.1.3 Glass Morphology

Figure 4.8 shows the change in the mean free path between crystals over time. The mean free path was observed to increase over time during crystal growth. Accordingly, as the microstructure coarsened and the crystals became larger, the glass regions between crystals also increased in size. This is contrary to the usual case. In most glass-ceramic systems, the mean free path decreases during crystal growth.
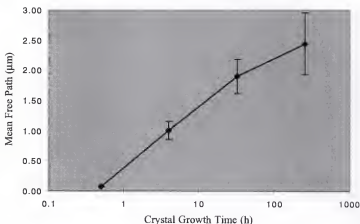
Figure 4.8. Effect of crystal growth time on the mean free path between crystals in BAS glass-ceramics.

4.2 Physical Properties

4.2.1 Density and Hardness

The mean apparent density values for materials with crystal growth times of 0, 0.5, 4, 32, and 256 h are summarized in Figure 4.9. One-way ANOVA showed that the

apparent density increased with increasing crystal growth time (p = 0.0001). A theoretical density of 3.941 g/cm³ was calculated for the hexacelsian crystals. According to the rule of mixtures, an increase from the initial glass density of 3.141 ± 0.004 g/cm³ to a density of 3.748 g/cm³ for the 0.5 h crystal growth treatment glass-ceramic was expected. Thereafter, the density was expected to remain constant because the crystalline volume fraction remained constant for longer crystal growth treatments. Instead, a slow continuous increase in density was observed. This may have been caused by the existence of internal porosity that was eliminated during high-temperature processing.

The mean hardness values for materials with crystal growth times of 0, 0.5, 4, 32, and 256 h are summarized in Figure 4.10. One-way ANOVA showed a significant difference in hardness between materials with different crystal growth times (p = 0.0001) with the highest hardness values corresponding to an intermediate (0.5 h) crystal growth time. The initial increase in hardness corresponds to the initial transformation of the lower hardness glass phase to the higher hardness crystal phase. For longer treatment times, the hardness decreases as the fraction of crystalline phase remains constant and the mean crystal size increases. Chyung *et al.* (1972) investigated mica-containing glass-ceramics which evolved microstructures similar to those observed in the present study. They reported that materials with a large mean crystal size exhibited lower hardness values because frictional sliding at the glass-mica interfaces allowed crushing to occur.
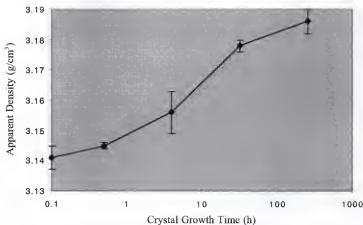
Figure 4.9. Effect of crystal growth time on the apparent density of BAS glass and glass-ceramics.
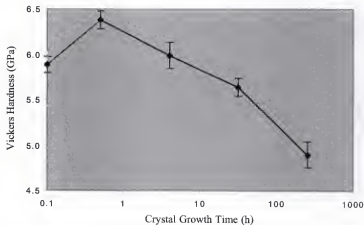
Figure 4.10. Effect of crystal growth time on the hardness of BAS glass and glass-ceramics.

4.2.2 Elastic Constants

Figure 4.11 shows the elastic moduli for BAS glass and glass-ceramics. Although the crystalline volume fraction remained constant, the Young's modulus, shear modulus, and bulk modulus increased with increasing crystal growth time. This may have been caused by an increase in the elastic anisotropy of BAS crystals with increasing crystal size. Likewise, there is a lack of single-crystal data in the existing literature. The only elastic moduli available are averaged over all the crystallographic directions because the microstructures of BAS glass-ceramics are fine. The inaccuracies resulting from averaging the elasticity of BAS crystals may become more evident at larger mean crystal sizes.
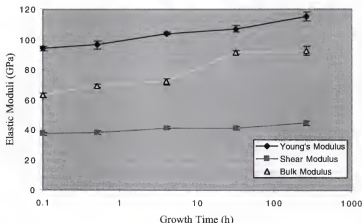
Figure 4.11. Effect of crystal growth time on Young's modulus, shear modulus, and bulk modulus of BAS glass and glass-ceramics.

4.2.3 Thermal Expansion

Push-rod dilatometry was used to measure the coefficient of thermal expansion for the base glass, which was 7.64 ppm/°C. Zhou *et al.* (1997) reported that the thermal expansion of hexacelsian glass-ceramic with 2% residual glass was 7.4 ppm/°C. Although the weak bonding along the basal (0001) cleavage plane suggests a higher thermal expansion coefficient along the [0001] direction of BAS crystals, the high mean crystal aspect ratio indicates that the maximum thermally induced strain occurs in <1000> directions.

4.2.4 Strength and Fracture Toughness

Figures 4.12 and 4.13 show the strength and fracture toughness, respectively, of BAS glass and glass-ceramics. Both strength and fracture toughness increase with increasing crystal growth time over the entire range of treatments investigated.

Because the measurements necessary for fracture toughness calculation via fractographic analysis require a great deal of skill and experience to collect accurately, two other methods were used to check the accuracy of the fractographic data. Comparison of the mean fracture toughness values calculated by the indentation strength technique (Section 3.3.6.2) and modified-indentation technique (Section 3.3.6.3) confirms the values calculated using fractographic analysis (Section 3.3.6.1). One-way ANOVA revealed no significant difference among the three toughness measurement methods ($p > 0.05$).
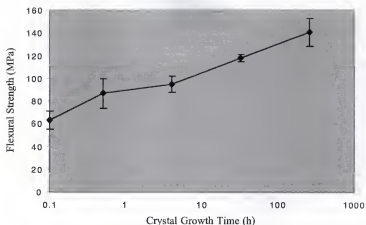
Figure 4.12. Effect of crystal growth time on the flexural strength of BAS glass and glass-ceramics.
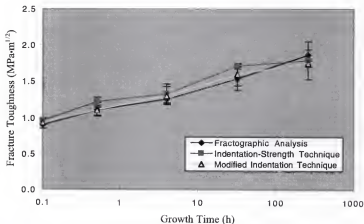
Figure 4.13. Effect of crystal growth time on the fracture toughness of BAS glass and glass-ceramics.

Uno *et al.* (1991) used glass with the same composition and similar thermal treatments to develop glass-ceramics with phlogopite as primary crystal phase. They reported strength and fracture toughness values of 350 MPa and 2.3 MPa·m$^{1/2}$, respectively, for a crystal growth treatment of 2 h at 1050°C. The difference between the observations of Uno *et al.* and those of the present study is more likely caused by a difference in test methods than a difference in crystal phase, because the phlogopite and BAS crystals have a similar structure and an identical morphology. Uno *et al.* measured strength using a three-point flexural test without a surface polish and without the introduction of a controlled flaw. Because the surface flaw population in their test specimens was not controlled, it is impossible to make a comparison between the strength values they reported and those observed in the present study. Uno *et al.* measured fracture toughness using a chevron-notched beam test, which can overestimate fracture toughness. Such an overestimate may be responsible for the large standard deviation they reported for the treatment group with the highest fracture toughness. Disregarding the suspect treatment group, the fracture toughness data of Uno *et al.* are similar to those observed in the present study and are well described by the predictions of Faber and Evans (1983a) for toughening caused by crack deflection.

4.3 Finite Element Predictions

Figure 4.14 shows the results of a finite element analysis that predicts the stress distribution surrounding BAS crystals embedded in a glass matrix. A tensile hoop stress and a compressive radial stress were predicted to develop in the matrix around each

crystal upon cooling from processing temperatures. Table 4.1 lists the maximum predicted principal stresses that result from each of the crystal growth treatments investigated. The stress fields associated with individual crystals overlap in the glass-ceramic crystallized for 0.5 h; however, the stress fields separated as the mean free path increased for longer crystal growth times. Actual stress magnitudes may be somewhat lower than those predicted because the corners of BAS crystals are not likely to be atomically sharp.
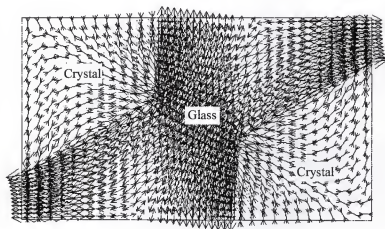
Figure 4.14. Residual stress field predicted by finite element analysis for a BAS glass-ceramic produced by a crystal growth time of 0.5 h. The vectors represent the magnitudes and directions of the principal stresses.

Table 4.1. Results of finite element analyses to predict the maximum stresses in BAS glass-ceramics.

Growth Time	1st Principal Stress*	2nd Principal Stress*	3rd Principal Stress†
0.5 h	14.4	2.74	6.13
4 h	10.2	1.92	21.9
32 h	10.5	2.05	21.8
256 h	11.3	2.13	27.5

*Stresses are given in MPa.

†Stresses are given in 10^{-4} MPa.

4.4 Strengthening and Toughening Mechanisms

4.4.1 Flaw Size Limitation

The theory of flaw size limitation (Hasselman and Fulrath, 1966) predicts that the strengths of glass-matrix composites vary inversely with the square-root of the mean free path between the reinforcing particles, *i.e.*, composite strength increases with decreasing mean free path. The opposite trend was observed for BAS glass-ceramics. Summarized in Table 4.2 are comparisons between the strength values predicted by the flaw size limitation theory with the experimental values. The observed flaw sizes were larger than those predicted by the theory of flaw size limitation (Equation 2.3); however, the strengths predicted for the observed flaw sizes can be calculated using the Griffith equation (2.1). The observed strengths were higher than those predicted by the Griffith equation. For BAS glass-ceramics and other fine-grained highly-crystalline glass-ceramics, the theory of flaw size limitation predicts composite strengths which are three orders of magnitude different from those observed. Flaw size limitation is not responsible for the

strengthening of these materials. Indeed, Mecholsky and Freiman (1980) reported that the mean flaw size increased instead of being limited for glass-ceramics with increased fracture toughness.

Table 4.2. Comparison of observed strength values with those predicted for flaws of limited size and flaws of observed size for BAS glass and glass-ceramics.

Growth Time	Predicted Strength For Limited Flaw Size[*]	Predicted Strength For Observed Flaw Size[*]	Observed Strength[*]		
0 h	63.4	63.4	63.4	±	8.0
0.5 h	2450	71.0	87.0	±	13.0
4 h	1790	72.4	94.8	±	7.0
32 h	1300	83.1	118	±	3
256 h	1010	76.0	141	±	12

[*]All strength values are given in MPa.

4.4.2 Crack Bowing

The theory of crack bowing (Lange, 1970; Evans, 1972; Green *et al.*, 1979) predicts that the strength of a glass-matrix composite will increase as the length of the subcritical crack front increases. The crack front length is a function of the mean free path between particles, the surface energy of the matrix, and the strength of the reinforcing particles. Figure 4.15 shows the relative strength increase predicted by the theory of crack bowing for the ratios of mean particle diameter to mean free path observed in BAS glass-ceramics. Glass-matrix composites that toughen through a coarsening reaction, such as BAS glass-ceramics, exhibit increased strength with increased mean free path. This is the opposite of the trend predicted when crack bowing is active. Also, the predictions of Green *et al.* do not fit the strengths observed for composites reinforced by brittle

particles, such as BAS crystals. A significant degree of bowing is more likely when the reinforcing particles are ductile, so crack bowing is not responsible for the strengthening of BAS glass-ceramics.
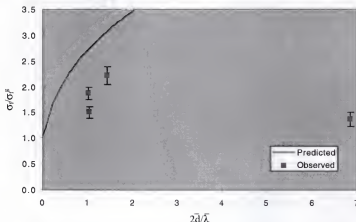
Figure 4.15. Comparison of the observed ratio of BAS glass-ceramic strength to base glass strength, σ_f/σ_f^g, with that predicted by the theory of crack bowing for the ratios of mean crystal diameter, $\overline{d}$, to mean free path, $\overline{\lambda}$.

4.4.3 Wake Process-Zone Mechanisms

When wake process-zone toughening mechanisms such as crack bridging, interfacial debonding, frictional pullout, stress-induced microcracking, and phase-transformation toughening (Sections 2.3.3 to 2.3.5) are active, fracture toughness increases with increasing flaw size because the wake process zone increases in length as a crack propagates through a material. Figure 4.16 shows the fracture toughness of BAS glass and glass-ceramics as a function of flaw size. The flaw sizes ranged from 44 to 98 μm for
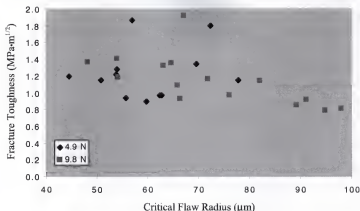
Figure 4.16. Effect of controlled flaw size on the fracture toughness of BAS glass and glass-ceramics. Controlled flaws were induced using a Vickers diamond under a load of 4.9 or 9.8 N.

indentation loads of 4.9 to 9.8 N, and fracture toughness was independent of indentation load ($p = 0.50$) over this range of flaw sizes. These data indicate that wake process-zone toughening mechanisms do not make a significant contribution to the fracture toughness of BAS glass-ceramics for the range of flaw sizes examined.

Crack bridging in particular should be visually evident when it is active in a composite. Figure 4.17 shows a BAS glass-ceramic specimen that was indented to produce radial cracks and acid-etched to reveal the microstructure surrounding these cracks. Visual examination revealed no intact reinforcements lying in the crack wake.
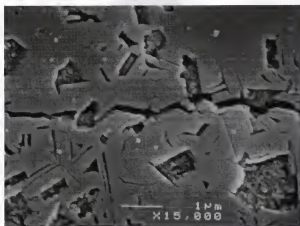
Figure 4.17. SEM micrograph of a radial crack (from a Vickers indentation induced under a load of 9.8 N) in a BAS glass-ceramic produced by crystal growth at 975°C for 32 h.
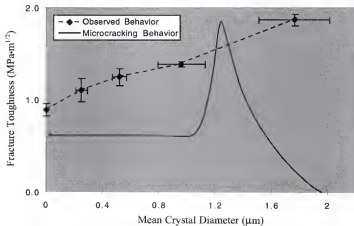
Figure 4.18. Observed effect of mean crystal diameter on the fracture toughness of BAS glass and glass-ceramics compared to that predicted by Rice and Freiman (1981).

Microcracking in particular should be strongly dependent on the size of the reinforcing crystals, within ±5% of a critical particle size (Rice and Freiman, 1981). Figure 4.18 shows the fracture toughness of BAS glass and glass-ceramics as a function of crystal diameter. Although mean crystal diameters ranged over an order of magnitude, a precipitous decrease in fracture toughness associated with spontaneous microcracking was not observed. The results of the finite element analysis presented in Figure 4.14 suggest a residual tensile hoop stress surrounding BAS crystals. Above a critical crystal diameter, this type of stress distribution results in radially-oriented microcracks which can be detrimental to glass-ceramic strength. However, the maximum tensile stress predicted for the largest crystals (1.76 μm in diameter) is only 11.3 MPa, much lower than the strength of the glass matrix (63.4 ± 8.0 MPa) for flaws larger than the mean crystal diameter. Thus, the critical crystal diameter must be much larger than the observed mean crystal diameter.

4.4.4 Stress Transfer

The theory of stress transfer (Frey and Mackenzie, 1967) predicts that the ratio of the strength of a glass-matrix composite to the strength of the base glass will increase in direct proportion to the ratio of the elastic moduli. Previous studies have verified the accuracy of this relation (Borom *et al.*, 1975; Borom, 1977; Swearengen *et al.*, 1978; Jessen *et al.*, 1986). Figure 4.19 shows the predicted and observed relative strengths of BAS glass-ceramics. BAS glass-ceramics were observed to follow the general trend predicted by stress transfer; however, stress transfer cannot account for all of the strength

increase that occurred. Jessen *et al.* reported similar results for glass reinforced with spherical Fe-Ni-Co alloy particles. Jessen *et al.* attributed the excess strength increase to crack deflection caused by residual thermally induced stress around the metal particles. Because the predicted contributions of stress transfer are well established, 100% of the strength increase attributed to this mechanism is expected for BAS glass-ceramics.
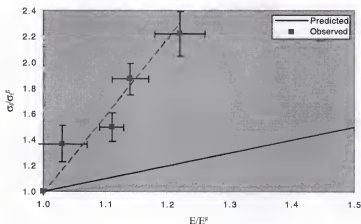
Figure 4.19. Comparison of the observed relationship between the ratio of composite strength to base glass strength, σ_f / σ_f^g, and the ratio of composite elastic modulus to base glass elastic modulus, E/E^g, with that predicted by the theory of stress transfer.

4.4.5 Crack Deflection

For reinforcing particles with a lower coefficient of thermal expansion than the matrix, the theory of crack deflection predicts that a crack will be deflected towards the particles, decreasing the stress intensity at the crack tip. This is the condition that exists in BAS glass-ceramics. Figures 4.20 to 4.23 show micrographs of BAS glass-ceramics
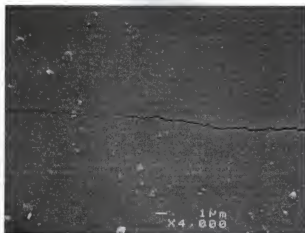
Figure 4.20. SEM micrograph of a radial crack from a Vickers indentation induced under a load of 9.8 N in a BAS glass-ceramic produced by crystal growth at 975°C for 0.5 h.

Figure 4.21. SEM micrograph of a radial crack from a Vickers indentation induced under a load of 9.8 N in a BAS glass-ceramic produced by crystal growth at 975°C for 4 h.
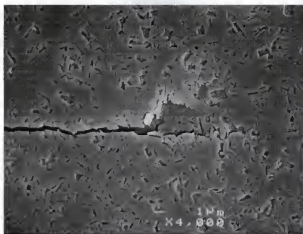
Figure 4.22. SEM micrograph of a radial crack from a Vickers indentation induced under a load of 9.8 N in a BAS glass-ceramic produced by crystal growth at 975°C for 32 h.
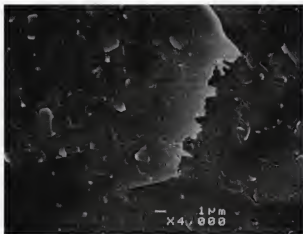
Figure 4.23. SEM micrograph of a radial crack from a Vickers indentation induced under a load of 9.8 N in a BAS glass-ceramic produced by crystal growth at 975°C for 256 h.

that were indented with a Vickers diamond under 9.8 N loads to produce radial cracks and subsequently acid-etched to reveal the microstructure surrounding these cracks. Crack deflection was visually confirmed in the glass-ceramic with the smallest mean crystal diameter (Figure 4.20). In the glass-ceramic with the largest mean crystal diameter (Figure 4.23), the crack front was observed to follow the interface, at some points turning perpendicular to the initial direction of propagation.

After subtracting the contribution of stress transfer, the remaining strength increase that must be accounted for by other mechanisms can be calculated. The toughness, $\mathcal{G}_C$, can be expressed in terms of the fracture toughness, K_{IC}, elastic modulus, E, failure stress, σ_f, and critical flaw size, c, as follows:

$$\mathcal{G}_C = \frac{K_{IC}^2}{E} = \frac{\left(Y\sigma_f\sqrt{c}\right)^2}{E} \tag{4.1}$$

The extra increase in normalized toughness can be expressed as

$$\Delta\mathcal{G}_{xs} = \frac{\mathcal{G}_{C,exp} - \mathcal{G}_{C,th}}{\mathcal{G}_C^g} \tag{4.2}$$

where $\mathcal{G}_{C,exp}$ is the experimentally observed toughness, $\mathcal{G}_{C,th}$ is the theoretical toughness caused by stress transfer, and $\mathcal{G}_C^g$ is the toughness of the base glass. Substitution of Equation 4.1 for the toughness values in Equation 4.2 yields the following equation for the extra increase in normalized toughness:

$$\Delta\mathcal{G}_{xs} = \frac{E^g\left(\sigma_{f,exp}^2 - \sigma_{f,th}^2\right)}{E\sigma_f^{g^2}} \tag{4.3}$$

where E is the elastic modulus of the glass-ceramic, E^t is the elastic modulus of the base glass, $\sigma_{f,exp}$ is the experimentally observed failure stress, $\sigma_{f,th}$ is the theoretical failure stress associated with stress transfer, and σ_f^t is the failure stress of the base glass.

Table 4.3 shows the normalized toughness increase observed for BAS glass-ceramics and the extra increase not accounted for by the contribution of stress transfer. Faber and Evans (1983) predicted a normalized toughness increase of 0.62 without crack front twisting and an increase of 1.43 with maximum twisting for disk-shaped plates with an aspect ratio of 3.0 (Figure 4.24). After subtracting the stress transfer contribution, the experimental data for BAS glass-ceramics show an increase in toughness within the range predicted by Faber and Evans. Table 4.4 shows the estimated relative contributions of stress transfer and crack deflection mechanisms to the observed strength increases. The relative contribution from crack deflection is larger for BAS glass-ceramics with a larger mean crystal size. This may be caused by an increase in the proportion of crack twisting versus crack tilting during crack deflection.

Table 4.3. Normalized toughness increase, $\Delta\mathcal{G}_c$, observed for BAS glass-ceramics and toughness increase not accounted for by the contribution of stress transfer, $\Delta\mathcal{G}_{xs}$.

Growth Time	$\Delta\mathcal{G}_c$	$\Delta\mathcal{G}_{xs}$
0.5 h	0.51	0.00
4 h	0.78	0.02
32 h	1.13	0.05
256 h	3.58	1.13
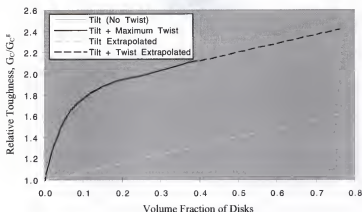
Figure 4.24. Prediction for the relative increase in fracture toughness associated with crack deflection by a dispersion of disk-shaped reinforcing particles (aspect ratio = 3) according to Faber and Evans (1983a).

Table 4.4. Estimated relative contributions of stress transfer and crack deflection mechanisms to the observed strengths of BAS glass-ceramics.

Growth Time	Stress Transfer	Crack Deflection
0.5 h	100%	0%
4 h	97%	3%
32 h	96%	4%
256 h	68%	32%

4.5 Process Optimization

The highest strength (141 ± 12 MPa) and fracture toughness (1.87 ± 0.07 MPa·m$^{1/2}$) were observed for the BAS glass-ceramic with the longest crystal growth time (256 h). This glass-ceramic also had the largest mean crystal diameter (1.76 ± 0.25 μm)

and the longest mean free path between crystals (2.44 ± 0.51 μm). The highest possible fracture toughness resulting from stress sharing and crack deflection mechanisms for this material is estimated to be 2.18 MPa·m$^{1/2}$. Fracture toughness was observed to increase with increasing mean crystal size over the entire range of glass-ceramics examined. This trend is expected to continue for larger crystal sizes without a decrease in fracture toughness caused by spontaneous microcracking. Finite element stress analyses predicted the maximum interfacial stress (11.3 MPa) to be much lower than the fracture stress of the base glass for a mean flaw radius of 76.6 μm (63.4 ± 8.0 MPa). Thus, only a 10.8% increase in interfacial stress was predicted for a 238% increase in crystal size. If this interfacial stress-size relationship continues linearly for larger crystals, then 60 μm would be the critical crystal diameter for the onset of spontaneous microcracking. This represents a 1150% increase in crystal size. Therefore, crystal growth treatments for BAS glass-ceramics should be carried out for as long as economically feasible.

The crystal growth temperature used in the present study was limited to 975°C in an effort to extend the lifetime of the chromel-alumel thermocouples in the tube furnace. An increase in crystal growth temperature is desirable for large-volume production of BAS glass-ceramics with large crystals, because the Arrhenius dependence of crystal growth rate on temperature causes an exponential increase in the crystal growth at higher temperatures. Pilot studies using differential thermal analysis estimated the energy barrier to crystallization for this glass composition to be 40 kJ/mol (Griggs and Anusavice,

1997). This indicates that the maximum crystal growth rate at higher treatment temperatures would be less than 3.14 times the crystal growth observed at 975°C.

Substitution of strontia for baria in the glass composition may decrease the processing temperature necessary to achieve rapid crystallization. Bansal *et al.* (1991) have explored the eutectic solubility that exists between barium aluminosilicate and strontium aluminosilicate. They found that partial substitution of baria with strontia produced the highest strength ceramics (96 to 103 MPa) at low processing temperatures (900°C). Care must be taken; however, to preserve the thermal compatibility between the glass phase ($\alpha = 7.64$ ppm/°C) and the hexacelsian crystal phase ($\alpha = 7.4$ ppm/°C). Bansal *et al.* reported that strontia substitution can change the primary crystal phase to monoclinic celsian ($\alpha = 2.1$ ppm/°C), which may result in spontaneous microcracking and a decrease in fracture toughness.

CHAPTER 5
CONCLUSIONS

The objectives of this study were to 1) determine which toughening mechanisms are active in the BAS glass-ceramic system, 2) estimate the relative contribution of each active mechanism to the increase in glass-ceramic strength and toughness over that of the base glass, and 3) identify a process for producing a glass-ceramic with the highest strength and fracture toughness.

Based on the results of this study, the following conclusions can be made:

1. Only toughening mechanisms that operate in the frontal process zone significantly increase the strength and fracture toughness of glass-ceramics containing BAS crystals with a mean diameter less than 1.76 µm. The lack of resistance-curve behavior excludes from consideration any mechanisms that operate solely within the wake process zone. Strengthening mechanisms that increase strength as the mean free path between reinforcements decreases are not active in BAS glass-ceramics.

2. Stress transfer is the primary mechanism responsible for an increase in BAS glass-ceramic strength. It can account for 68% of the observed strengthening, for glass-ceramics with coarse microstructures, and 100% of the observed strengthening, for glass-ceramics with fine microstructures. Crack deflection is the secondary

mechanism responsible for the remainder of the observed strengthening in glass-ceramics with the coarsest microstructures.

3. The strength and fracture toughness of BAS glass-ceramics increased with increasing duration of crystal growth treatment over the entire range of durations investigated. To achieve the highest possible strength and fracture toughness, the glass should be processed at temperatures in excess of 975°C for as long as economically feasible.

A.1 Model of Glass-Ceramic Subjected to Crystal Growth for 0.5 h

```
/BATCH
/input,menust,tmp    ,,,,,,,,,,,,,,1
/PREP7
K,,,,,
K,,0.125e-3,,,
K,,0.16e-3,,,
K,,0.16e-3,0.1083e-3,,
K,,0.0625e-3,0.1083e-3,,
K,,0.0e-3,0.1083e-3,,
K,,0.0e-3,0.1689e-3,,
K,,0.0975e-3,0.1689e-3,,
K,,0.16e-3,0.1689e-3,,
K,,0.16e-3,0.2771e-3,,
K,,0.035e-3,0.2771e-3,,
K,,0.0e-3,0.2771e-3,,
LSTR,    11,    10
LSTR,    10,    9
LSTR,    9,    8
LSTR,    8,    11
LSTR,    6,    5
LSTR,    5,    2
LSTR,    2,    1
LSTR,    1,    6
FLST,2,4,4
FITEM,2,1
FITEM,2,4
FITEM,2,2
FITEM,2,3
AL,P51X
FLST,2,4,4
FITEM,2,5
FITEM,2,6
```

```
FITEM,2,8
FITEM,2,7
AL,P51X
LSLA
KSLL
NSLA,,1
ESLN,,1
CM,cryst-l,LINE
CM,cryst-k,KP
CM,cryst-a,AREA
VSEL,ALL
ASEL,ALL
LSEL,ALL
KSEL,ALL
ESEL,ALL
NSEL,ALL
FLST,3,6,3,ORDE,6
FITEM,3,2
FITEM,3,5
FITEM,3,-6
FITEM,3,8
FITEM,3,-9
FITEM,3,11
KGEN,2,P51X, , , , , , ,0
CMSEL,U,CRYST-A
CMSEL,U,CRYST-K
CMSEL,U,CRYST-L
LSTR,    12,    18
LSTR,    18,    16
LSTR,    16,    17
LSTR,    17,     4
LSTR,     4,     3
LSTR,     3,    13
LSTR,    13,    14
LSTR,    14,    15
LSTR,    15,     7
LSTR,     7,    12
LSTR,     7,    16
LSTR,    16,    14
LSTR,    14,     4
FLST,2,4,4
FITEM,2,18
FITEM,2,9
```

```
FITEM,2,10
FITEM,2,19
AL,P51X
FLST,2,4,4
FITEM,2,19
FITEM,2,20
FITEM,2,17
FITEM,2,16
AL,P51X
FLST,2,4,4
FITEM,2,20
FITEM,2,11
FITEM,2,21
FITEM,2,12
AL,P51X
FLST,2,4,4
FITEM,2,21
FITEM,2,15
FITEM,2,13
FITEM,2,14
AL,P51X
CM,matrix-a,AREA
CM,matrix-l,LINE
CM,matrix-k,KP
VSEL,ALL
ASEL,ALL
LSEL,ALL
KSEL,ALL
ESEL,ALL
NSEL,ALL
ET,1,PLANE82
UIMP,1,EX, , ,94000,
UIMP,1,DENS, , , ,
UIMP,1,ALPX, , ,7.6e-6,
UIMP,1,REFT, , , ,
UIMP,1,NUXY, , ,0.28,
UIMP,1,PRXY, , , ,
UIMP,1,GXY, , , ,
UIMP,1,DAMP, , , ,
UIMP,2,EX, , ,110000,
UIMP,2,DENS, , , ,
UIMP,2,ALPX, , ,7.4e-6,
UIMP,2,REFT, , , ,
```

```
UIMP,2,NUXY, , ,0.26,
UIMP,2,PRXY, , , , ,
UIMP,2,GXY, , , , ,
UIMP,2,DAMP, , , ,
FLST,2,21,4,ORDE,2
FITEM,2,1
FITEM,2,-21
LESIZE,P51X, , ,12,1,
FLST,5,4,5,ORDE,2
FITEM,5,3
FITEM,5,-6
CM,_Y,AREA
ASEL, , , ,P51X
CM,_Y1,AREA
CHKMSH,'AREA'
CMSEL,S,_Y
ESHAPE,2,0
AMESH,_Y1
ESHAPE,0,0
CMDEL,_Y
CMDEL,_Y1
CMDEL,_Y2
CM,matrix-e,ELEM
CM,matrix-n,NODE
CMGRP,matrix,MATRIX-A,MATRIX-E,MATRIX-K,MATRIX-L,MATRIX-N
CMSEL,U,MATRIX
TYPE,1,
MAT,2,
REAL,1,
ESYS,0,
FLST,5,2,5,ORDE,2
FITEM,5,1
FITEM,5,-2
CM,_Y,AREA
ASEL, , , ,P51X
CM,_Y1,AREA
CHKMSH,'AREA'
CMSEL,S,_Y
ESHAPE,2,0
AMESH,_Y1
ESHAPE,0,0
CMDEL,_Y
CMDEL,_Y1
```

```
CMDEL,_Y2
CM,cryst-n,NODE
CM,cryst-e,ELEM
CMGRP,crystal,CRYST-A,CRYST-E,CRYST-K,CRYST-L,CRYST-N
VSEL,ALL
ASEL,ALL
LSEL,ALL
KSEL,ALL
ESEL,ALL
NSEL,ALL
FLST,4,50,1,ORDE,5
FITEM,4,2
FITEM,4,26
FITEM,4,-49
FITEM,4,1850
FITEM,4,-1874
CP,1,UY,P51X
FLST,4,74,1,ORDE,8
FITEM,4,938
FITEM,4,962
FITEM,4,-985
FITEM,4,1394
FITEM,4,-1417
FITEM,4,1851
FITEM,4,1875
FITEM,4,-1898
CP,2,UX,P51X
FLST,5,4,1,ORDE,4
FITEM,5,26
FITEM,5,962
FITEM,5,1850
FITEM,5,1875
NSEL,U, , ,P51X
CPINTF,ALL,1e-7,
VSEL,ALL
ASEL,ALL
LSEL,ALL
KSEL,ALL
ESEL,ALL
NSEL,ALL
FLST,5,2,1,ORDE,2
FITEM,5,26
FITEM,5,1850
```

```
NSEL,S, , ,P51X
FLST,5,2,1,ORDE,2
FITEM,5,26
FITEM,5,1850
NSEL,S, , ,P51X
CPINTF,UX,1e-07,
VSEL,ALL
ASEL,ALL
LSEL,ALL
KSEL,ALL
ESEL,ALL
NSEL,ALL
FLST,5,2,1,ORDE,2
FITEM,5,962
FITEM,5,1875
NSEL,S, , ,P51X
CPINTF,UY,1e-07,
VSEL,ALL
ASEL,ALL
LSEL,ALL
KSEL,ALL
ESEL,ALL
NSEL,ALL
FINISH
/SOLU
TUNIF,577,
TREF,577,
FLST,2,74,1,ORDE,9
FITEM,2,1
FITEM,2,-25
FITEM,2,506
FITEM,2,530
FITEM,2,-552
FITEM,2,2331
FITEM,2,2380
FITEM,2,2404
FITEM,2,-2426
D,P51X, ,0, , , ,UX
FLST,2,50,1,ORDE,6
FITEM,2,1394
FITEM,2,1418
FITEM,2,-1441
FITEM,2,2356
```

```
FITEM,2,2380
FITEM,2,-2403
D,P51X, ,0, , , ,UY
FLST,2,2811,1,ORDE,2
FITEM,2,1
FITEM,2,-2811
BF,P51X,TEMP,0,
SOLVE
FINISH
/POST1
SET,LAST
CMSEL,S,MATRIX
VSEL,ALL
ASEL,ALL
LSEL,ALL
KSEL,ALL
ESEL,ALL
NSEL,ALL
FINISH
```

A.2 Model of Glass-Ceramic Subjected to Crystal Growth for 4 h

```
/BATCH
/input,menust,tmp    ,,,,,,,,,,,,1
/PREP7
K, ,,,,
K, ,0.26e-3,,,
K, ,0.765e-3,,,
K, ,0.765e-3,0.2252e-3,,
K, ,0.13e-3,0.2252e-3,,
K, ,0.0e-3,0.2252e-3,,
K, ,0.0e-3,1.1e-3,,
K, ,0.635e-3,1.1e-3,,
K, ,0.765e-3,1.1e-3,,
K, ,0.0e-3,1.325e-3,,
K, ,0.505e-3,1.325e-3,,
K, ,0.765e-3,1.325e-3,,
LSTR,    11,    12
LSTR,    12,     9
LSTR,     9,     8
LSTR,     8,    11
LSTR,     6,     5
```

```
LSTR,    5,    2
LSTR,    2,    1
LSTR,    1,    6
FLST,2,4,4
FITEM,2,1
FITEM,2,4
FITEM,2,2
FITEM,2,3
AL,P51X
FLST,2,4,4
FITEM,2,5
FITEM,2,8
FITEM,2,7
FITEM,2,6
AL,P51X
LSLA
KSLL
NSLA,,1
ESLN,,1
CM,cryst-a,AREA
CM,cryst-l,LINE
CM,cryst-k,KP
VSEL,ALL
ASEL,ALL
LSEL,ALL
KSEL,ALL
ESEL,ALL
NSEL,ALL
FLST,3,6,3,ORDE,6
FITEM,3,2
FITEM,3,5
FITEM,3,-6
FITEM,3,8
FITEM,3,-9
FITEM,3,11
KGEN,2,P51X, , , , , , ,0
CMSEL,U,CRYST-A
CMSEL,U,CRYST-K
CMSEL,U,CRYST-L
LSTR,   10,   18
LSTR,   18,   16
LSTR,   16,    7
LSTR,    7,   10
```

```
LSTR,    16,    17
LSTR,    17,     4
LSTR,    16,    14
LSTR,    14,     4
LSTR,     7,    15
LSTR,    15,    14
LSTR,    14,    13
LSTR,    13,     3
LSTR,     3,     4
FLST,2,4,4
FITEM,2,9
FITEM,2,11
FITEM,2,10
FITEM,2,12
AL,P51X
FLST,2,4,4
FITEM,2,11
FITEM,2,18
FITEM,2,15
FITEM,2,17
AL,P51X
FLST,2,4,4
FITEM,2,15
FITEM,2,13
FITEM,2,14
FITEM,2,16
AL,P51X
FLST,2,4,4
FITEM,2,16
FITEM,2,20
FITEM,2,19
FITEM,2,21
AL,P51X
CM,matrix-k,KP
CM,matrix-l,LINE
CM,matrix-a,AREA
VSEL,ALL
ASEL,ALL
LSEL,ALL
KSEL,ALL
ESEL,ALL
NSEL,ALL
ET,1,PLANE82
```

```
KEYOPT,1,3,0
KEYOPT,1,5,0
KEYOPT,1,6,0
UIMP,1,EX, ,94000,
UIMP,1,DENS, , , ,
UIMP,1,ALPX, , ,7.6e-6,
UIMP,1,REFT, , , ,
UIMP,1,NUXY, , ,0.28,
UIMP,1,PRXY, , , ,
UIMP,1,GXY, , , ,
UIMP,1,DAMP, , , ,
UIMP,2,EX, , ,110000,
UIMP,2,DENS, , , ,
UIMP,2,ALPX, , ,7.4e-3,
UIMP,2,REFT, , , ,
UIMP,2,NUXY, , ,0.26,
UIMP,2,PRXY, , , ,
UIMP,2,GXY, , , ,
UIMP,2,DAMP, , , ,
ESHAPE,2,0
LESIZE,ALL, , ,10,1,1
FLST,2,3,4,ORDE,3
FITEM,2,14
FITEM,2,-15
FITEM,2,17
LESIZE,P51X, , ,16,1,
FLST,2,3,4,ORDE,3
FITEM,2,14
FITEM,2,-15
FITEM,2,17
LESIZE,P51X, , ,20,1,
FLST,2,2,4,ORDE,2
FITEM,2,16
FITEM,2,20
LESIZE,P51X, , ,10,2,
FLST,2,2,4,ORDE,2
FITEM,2,16
FITEM,2,20
LESIZE,P51X, , ,10,3,
FLST,2,2,4,ORDE,2
FITEM,2,9
FITEM,2,11
LESIZE,P51X, , ,10,3,
```

```
FLST,2,1,4,ORDE,1
FITEM,2,9
LESIZE,P51X, , ,10,0.33333,
FLST,2,3,4,ORDE,3
FITEM,2,11
FITEM,2,16
FITEM,2,20
LESIZE,P51X, , ,10,4,
FLST,2,1,4,ORDE,1
FITEM,2,9
LESIZE,P51X, , ,10,0.25,
TYPE,1,
MAT,1,
REAL,1,
ESYS,0,
FLST,5,4,5,ORDE,2
FITEM,5,3
FITEM,5,-6
CM,_Y,AREA
ASEL, , , ,P51X
CM,_Y1,AREA
CHKMSH,'AREA'
CMSEL,S,_Y
AMESH,_Y1
CMDEL,_Y
CMDEL,_Y1
CMDEL,_Y2
CM,matrix-e,ELEM
CM,matrix-n,NODE
CMGRP,matrix,MATRIX-A,MATRIX-E,MATRIX-K,MATRIX-L,MATRIX-N
TYPE,1,
MAT,2,
REAL,1,
ESYS,0,
FLST,5,2,5,ORDE,2
FITEM,5,1
FITEM,5,-2
CM,_Y,AREA
ASEL, , , ,P51X
CM,_Y1,AREA
CHKMSH,'AREA'
CMSEL,S,_Y
AMESH,_Y1
```

```
CMDEL,_Y
CMDEL,_Y1
CMDEL,_Y2
CMSEL,U,MATRIX
CM,cryst-n,NODE
CM,cryst-e,ELEM
CMGRP,crystal,CRYST-A,CRYST-E,CRYST-K,CRYST-L,CRYST-N
VSEL,ALL
ASEL,ALL
LSEL,ALL
KSEL,ALL
ESEL,ALL
NSEL,ALL
FLST,5,4,1,ORDE,4
FITEM,5,2
FITEM,5,1002
FITEM,5,1922
FITEM,5,1943
NSEL,U, , ,P51X
CPINTF,ALL,1e-6,
FLST,4,40,1,ORDE,5
FITEM,4,1
FITEM,4,3
FITEM,4,-21
FITEM,4,1923
FITEM,4,-1942
CP,1,UY,P51X
FLST,4,80,1,ORDE,8
FITEM,4,982
FITEM,4,1003
FITEM,4,-1041
FITEM,4,1602
FITEM,4,-1621
FITEM,4,1923
FITEM,4,1944
FITEM,4,-1962
CP,2,UX,P51X
VSEL,ALL
ASEL,ALL
LSEL,ALL
KSEL,ALL
ESEL,ALL
NSEL,ALL
```

```
FLST,5,2,1,ORDE,2
FITEM,5,2
FITEM,5,1922
NSEL,S, , ,P51X
VSEL,ALL
ASEL,ALL
LSEL,ALL
KSEL,ALL
ESEL,ALL
NSEL,ALL
CPDELE,1,2,,ANY
FLST,4,42,1,ORDE,4
FITEM,4,1
FITEM,4,-21
FITEM,4,1922
FITEM,4,-1942
CP,1,UY,P51X
FLST,4,82,1,ORDE,8
FITEM,4,982
FITEM,4,1002
FITEM,4,-1041
FITEM,4,1602
FITEM,4,-1621
FITEM,4,1923
FITEM,4,1943
FITEM,4,-1962
CP,2,UX,P51X
FLST,5,2,1,ORDE,2
FITEM,5,2
FITEM,5,1922
NSEL,S, , ,P51X
CPINTF,UX,1e-06,
VSEL,ALL
ASEL,ALL
LSEL,ALL
KSEL,ALL
ESEL,ALL
NSEL,ALL
FLST,5,2,1,ORDE,2
FITEM,5,1002
FITEM,5,1943
NSEL,S, , ,P51X
CPINTF,UY,1e-06,
```

```
VSEL,ALL
ASEL,ALL
LSEL,ALL
KSEL,ALL
ESEL,ALL
NSEL,ALL
FINISH
/SOLU
FLST,2,82,1,ORDE,10
FITEM,2,I
FITEM,2,42
FITEM,2,62
FITEM,2,-80
FITEM,2,342
FITEM,2,-381
FITEM,2,2263
FITEM,2,2304
FITEM,2,2324
FITEM,2,-2342
D,P51X,,0,,,,UX
FLST,2,42,1,ORDE,6
FITEM,2,1602
FITEM,2,1622
FITEM,2,-1641
FITEM,2,2284
FITEM,2,2304
FITEM,2,-2323
D,P51X,,0,,,,UY
TUNIF,577,
TREF,0,
FLST,2,2603,1,ORDE,2
FITEM,2,1
FITEM,2,-2603
BF,P51X,TEMP,0,
SOLVE
FINISH
/POST1
SET,LAST
FINISH
/SOLU
FINISH
/PREP7
VSEL,ALL
```

```
ASEL,ALL
LSEL,ALL
KSEL,ALL
ESEL,ALL
NSEL,ALL
FINISH
/SOLU
TUNIF,577,
TREF,577,
FLST,2,2603,1,ORDE,2
FITEM,2,1
FITEM,2,-2603
BF,P51X,TEMP,0,
SOLVE
FINISH
/POST1
SET,LAST
CMSEL,S,MATRIX
FINISH
VSEL,ALL
ASEL,ALL
LSEL,ALL
KSEL,ALL
ESEL,ALL
NSEL,ALL
/PREP7
FINISH
/POST1
SET,LAST
FINISH
/SOLU
ANTYPE,0
TUNIF,577,
TREF,577,
FLST,2,2603,1,ORDE,2
FITEM,2,1
FITEM,2,-2603
BF,P51X,TEMP,0,
SOLVE
FINISH
/POST1
SET,LAST
FINISH
```

```
/PREP7
FINISH
/POST1
CMSEL,S,MATRIX
/PREP7
UIMP,2,EX, , ,110000,
UIMP,2,DENS, , , ,
UIMP,2,ALPX, , ,7.4e-6,
UIMP,2,REFT, , , ,
UIMP,2,NUXY, , ,0.26,
UIMP,2,PRXY, , , ,
UIMP,2,GXY, , , ,
UIMP,2,DAMP, , , ,
VSEL,ALL
ASEL,ALL
LSEL,ALL
KSEL,ALL
ESEL,ALL
NSEL,ALL
FINISH
```

A.3 Model of Glass-Ceramic Subjected to Crystal Growth for 32 h

```
/BATCH
/input,menust,tmp    ,,,,,,,,,,,,,,1
/PREP7
K, ,,,,
K, ,0.48e-3,,,
K, ,1.43e-3,,,
K, ,1.43e-3,0.4157e-3,,
K, ,0.24e-3,0.4157e-3,,
K, ,0.0e-3,0.4157e-3,,
K, ,0.0e-3,2.0611e-3,,
K, ,0.1.16e-3,2.0611e-3,,
K,8,1.16e-3,2.0611e-3,,
K,8,1.43e-3,2.0611e-3,,
K,8,1.43e-3,2.477e-3,,
K,8,1.16e-3,2.0611e-3,,
K, ,1.43e-3,2.0611e-3,,
K, ,1.43e-3,2.477e-3,,
K, ,0.95e-3,2.477e-3,,
K, ,0.e-3,2.477e-3,,
```

```
LSTR,    11,    10
LSTR,    10,     9
LSTR,     9,     8
LSTR,     8,    11
LSTR,     6,     5
LSTR,     5,     2
LSTR,     2,     1
LSTR,     1,     6
FLST,2,4,4
FITEM,2,1
FITEM,2,4
FITEM,2,2
FITEM,2,3
AL,P51X
FLST,2,4,4
FITEM,2,5
FITEM,2,6
FITEM,2,8
FITEM,2,7
AL,P51X
LSLA
KSLL
NSLA,,1
ESLN,,1
CM,cryst-a,AREA
CM,cryst-l,LINE
CM,cryst-k,KP
VSEL,ALL
ASEL,ALL
LSEL,ALL
KSEL,ALL
ESEL,ALL
NSEL,ALL
FLST,3,6,3,ORDE,6
FITEM,3,2
FITEM,3,5
FITEM,3,-6
FITEM,3,8
FITEM,3,-9
FITEM,3,11
KGEN,2,P51X, , , , , , ,0
CMSEL,U,CRYST-A
CMSEL,U,CRYST-K
```

```
CMSEL,U,CRYST-L
LSTR,    12,    18
LSTR,    18,    16
LSTR,    16,     7
LSTR,    12,     7
LSTR,    16,    17
LSTR,    17,     4
LSTR,    16,    14
LSTR,    14,     4
LSTR,     7,    15
LSTR,    15,    14
LSTR,    14,    13
LSTR,    13,     3
LSTR,     3,     4
FLST,2,4,4
FITEM,2,9
FITEM,2,11
FITEM,2,12
FITEM,2,10
AL,P51X
FLST,2,4,4
FITEM,2,11
FITEM,2,15
FITEM,2,17
FITEM,2,18
AL,P51X
FLST,2,4,4
FITEM,2,13
FITEM,2,15
FITEM,2,14
FITEM,2,16
AL,P51X
FLST,2,4,4
FITEM,2,20
FITEM,2,16
FITEM,2,19
FITEM,2,21
AL,P51X
LSLA
KSLL
NSLA,,1
ESLN,,1
CM,matrix-k,KP
```

```
CM,matrix-l,LINE
CM,matrix-a,AREA
VSEL,ALL
ASEL,ALL
LSEL,ALL
KSEL,ALL
ESEL,ALL
NSEL,ALL
ET,1,PLANE82
UIMP,1,EX, , ,94000,
UIMP,1,DENS, , , ,
UIMP,1,ALPX, , ,7.6e-6,
UIMP,1,REFT, , , ,
UIMP,1,NUXY, , ,0.28,
UIMP,1,PRXY, , , ,
UIMP,1,GXY, , , ,
UIMP,1,DAMP, , , ,
UIMP,2,EX, , ,110000,
UIMP,2,DENS, , , ,
UIMP,2,ALPX, , ,7.4e-6,
UIMP,2,REFT, , , ,
UIMP,2,NUXY, , ,0.26,
UIMP,2,PRXY, , , ,
UIMP,2,GXY, , , ,
UIMP,2,DAMP, , , ,
LESIZE,ALL, , ,10,1,1
FLST,2,3,4,ORDE,3
FITEM,2,14
FITEM,2,-15
FITEM,2,17
LESIZE,P51X, , ,20,1,
FLST,2,2,4,ORDE,2
FITEM,2,16
FITEM,2,20
LESIZE,P51X, , ,10,4,
FLST,2,2,4,ORDE,2
FITEM,2,9
FITEM,2,11
LESIZE,P51X, , ,10,4,
FLST,2,1,4,ORDE,1
FITEM,2,9
LESIZE,P51X, , ,10,0.25,
FLST,5,4,5,ORDE,2
```

```
FITEM,5,3
FITEM,5,-6
CM,_Y,AREA
ASEL, , , ,P51X
CM,_Y1,AREA
CHKMSH,'AREA'
CMSEL,S,_Y
ESHAPE,2,0
AMESH,_Y1
ESHAPE,0,0
CMDEL,_Y
CMDEL,_Y1
CMDEL,_Y2
CM,matrix-e,ELEM
CM,matrix-n,ELEM
TYPE,1,
MAT,2,
REAL,1,
ESYS,0,
FLST,5,2,5,ORDE,2
FITEM,5,1
FITEM,5,-2
CM,_Y,AREA
ASEL, , , ,P51X
CM,_Y1,AREA
CHKMSH,'AREA'
CMSEL,S,_Y
ESHAPE,2,0
AMESH,_Y1
ESHAPE,0,0
CMDEL,_Y
CMDEL,_Y1
CMDEL,_Y2
CMGRP,matrix,MATRIX-A,MATRIX-E,MATRIX-K,MATRIX-L,MATRIX-N
CMSEL,U,MATRIX
CM,cryst-e,ELEM
VSEL,ALL
ASEL,ALL
LSEL,ALL
KSEL,ALL
ESEL,ALL
NSEL,ALL
FLST,5,4,5,ORDE,2
```

```
FITEM,5,3
FITEM,5,-6
ASEL,S, , ,P51X
LSLA
KSLL
NSLA,,1
ESLN,,1
CM,matrix-n,NODE
CMDELE,MATRIX
CMGRP,matrix,MATRIX-A,MATRIX-E,MATRIX-K,MATRIX-L,MATRIX-N
VSEL,ALL
ASEL,ALL
LSEL,ALL
KSEL,ALL
ESEL,ALL
NSEL,ALL
CMSEL,U,MATRIX
CM,cryst-n,NODE
CMGRP,crystal,CRYST-A,CRYST-E,CRYST-K,CRYST-L,CRYST-N
VSEL,ALL
ASEL,ALL
LSEL,ALL
KSEL,ALL
ESEL,ALL
NSEL,ALL
FINISH
/SOLU
FINISH
/PREP7
FLST,4,42,1,ORDE,4
FITEM,4,1
FITEM,4,-21
FITEM,4,1922
FITEM,4,-1942
CP,1,UY,P51X
FLST,4,82,1,ORDE,9
FITEM,4,982
FITEM,4,1002
FITEM,4,-1041
FITEM,4,1603
FITEM,4,1623
FITEM,4,-1641
FITEM,4,1923
```

```
FITEM,4,1943
FITEM,4,-1962
CP,2,UX,P51X
FLST,5,4,1,ORDE,4
FITEM,5,2
FITEM,5,982
FITEM,5,1922
FITEM,5,1943
NSEL,U, , ,P51X
CPINTF,ALL,1e-6,
VSEL,ALL
ASEL,ALL
LSEL,ALL
KSEL,ALL
ESEL,ALL
NSEL,ALL
FLST,5,2,1,ORDE,2
FITEM,5,2
FITEM,5,1922
NSEL,U, , ,P51X
CPINTF,UX,1e-06,
VSEL,ALL
ASEL,ALL
LSEL,ALL
KSEL,ALL
ESEL,ALL
NSEL,ALL
FLST,5,2,1,ORDE,2
FITEM,5,2
FITEM,5,1922
NSEL,S, , ,P51X
FLST,5,2,1,ORDE,2
FITEM,5,2
FITEM,5,1922
NSEL,S, , ,P51X
CPINTF,UX,1e-06,
VSEL,ALL
ASEL,ALL
LSEL,ALL
KSEL,ALL
ESEL,ALL
NSEL,ALL
FLST,5,2,1,ORDE,2
```

```
FITEM,5,982
FITEM,5,1943
NSEL,S, , ,P51X
CPINTF,UY,1e-06,
VSEL,ALL
ASEL,ALL
LSEL,ALL
KSEL,ALL
ESEL,ALL
NSEL,ALL
FINISH
/SOLU
TUNIF,577,
TUNIF,577,
TREF,577,
FLST,2,82,1,ORDE,10
FITEM,2,1
FITEM,2,42
FITEM,2,62
FITEM,2,-80
FITEM,2,342
FITEM,2,-381
FITEM,2,2263
FITEM,2,2304
FITEM,2,2324
FITEM,2,-2342
D,P51X, ,0, , , ,UX
FLST,2,42,1,ORDE,5
FITEM,2,1602
FITEM,2,-1622
FITEM,2,2284
FITEM,2,2304
FITEM,2,-2323
D,P51X, ,0, , , ,UY
FLST,2,2603,1,ORDE,2
FITEM,2,1
FITEM,2,-2603
BF,P51X,TEMP,0,
SOLVE
FINISH
/PREP7
CPDELE,3,100000,,ANY
FLST,5,4,1,ORDE,4
```

```
FITEM,5,2
FITEM,5,982
FITEM,5,1922
FITEM,5,1943
NSEL,U, , ,P51X
CPINTF,ALL,1e-06,
VSEL,ALL
ASEL,ALL
LSEL,ALL
KSEL,ALL
ESEL,ALL
NSEL,ALL
FLST,5,2,1,ORDE,2
FITEM,5,2
FITEM,5,1922
NSEL,S, , ,P51X
CPINTF,UY,1e-06,
CPDELE,406,406,,ANY
CPINTF,UX,1e-06,
VSEL,ALL
ASEL,ALL
LSEL,ALL
KSEL,ALL
ESEL,ALL
NSEL,ALL
FLST,5,2,1,ORDE,2
FITEM,5,982
FITEM,5,1943
NSEL,S, , ,P51X
CPINTF,UY,1e-06,
VSEL,ALL
ASEL,ALL
LSEL,ALL
KSEL,ALL
ESEL,ALL
NSEL,ALL
FINISH
/SOLU
SOLVE
FINISH
/POST1
SET,LAST
CMSEL,U,MATRIX
```

```
CMSEL,S,MATRIX
VSEL,ALL
ASEL,ALL
LSEL,ALL
KSEL,ALL
ESEL,ALL
NSEL,ALL
CMSEL,S,CRYSTAL
VSEL,ALL
ASEL,ALL
LSEL,ALL
KSEL,ALL
ESEL,ALL
NSEL,ALL
```

A.4 Model of Glass-Ceramic Subjected to Crystal Growth for 256 h

```
/BATCH
/input,menust,tmp   ,,,,,,,,,,,,,,,1
/PREP7
K, ,,,,
K, ,0.88e-3,,,
K, ,2.1e-3,,,
K, ,2.1e-3,0.7621e-3,,
K, ,0.44e-3,0.7621e-3,,
K, ,0.e-3,0.7621e-3,,
K, ,0.e-3,3.024e-3,,
K, ,1.66e-3,3.024e-3,,
K, ,2.1e-3,3.024e-3,,
K, ,2.1e-3,2.1e-3,,
K,10,2.1e-3,3.6373e-3,,
K, ,1.22e-3,3.6373e-3,,
K, ,0e-3,3.6373e-3,,
LSTR,   11,    8
LSTR,    8,    9
LSTR,    9,   10
LSTR,   10,   11
LSTR,    6,    5
LSTR,    5,    2
LSTR,    2,    1
LSTR,    1,    6
FLST,2,4,4
```

```
FITEM,2,4
FITEM,2,3
FITEM,2,1
FITEM,2,2
AL,P51X
FLST,2,4,4
FITEM,2,5
FITEM,2,6
FITEM,2,8
FITEM,2,7
AL,P51X
LSLA
KSLL
NSLA,,1
ESLN,,1
CM,cryst-a,AREA
CM,cryst-l,LINE
CM,cryst-k,KP
FLST,3,6,3,ORDE,6
FITEM,3,2
FITEM,3,5
FITEM,3,-6
FITEM,3,8
FITEM,3,-9
FITEM,3,11
KGEN,2,P51X, , , , , , ,0
CMSEL,U,CRYST-A
CMSEL,U,CRYST-K
CMSEL,U,CRYST-L
VSEL,ALL
ASEL,ALL
LSEL,ALL
KSEL,ALL
ESEL,ALL
NSEL,ALL
CMSEL,U,CRYST-L
CMSEL,U,CRYST-K
CMSEL,U,CRYST-A
LSTR,    12,    18
LSTR,    18,    16
LSTR,    16,     7
LSTR,     7,    12
LSTR,    16,    17
```

```
LSTR,    17,    4
LSTR,    16,   14
LSTR,    14,    4
LSTR,     7,   15
LSTR,    15,   14
LSTR,    14,   13
LSTR,    13,    3
LSTR,     3,    4
FLST,2,4,4
FITEM,2,9
FITEM,2,11
FITEM,2,12
FITEM,2,10
AL,P51X
FLST,2,4,4
FITEM,2,17
FITEM,2,11
FITEM,2,15
FITEM,2,18
AL,P51X
FLST,2,4,4
FITEM,2,15
FITEM,2,14
FITEM,2,13
FITEM,2,16
AL,P51X
FLST,2,4,4
FITEM,2,16
FITEM,2,20
FITEM,2,19
FITEM,2,21
AL,P51X
CM,matrix-k,KP
CM,matrix-l,LINE
CM,matrix-a,AREA
VSEL,ALL
ASEL,ALL
LSEL,ALL
KSEL,ALL
ESEL,ALL
NSEL,ALL
ET,1,PLANE82
KEYOPT,1,3,0
```

```
KEYOPT,1,5,0
KEYOPT,1,6,0
UIMP,1,EX, , ,94000,
UIMP,1,DENS, , , ,
UIMP,1,ALPX, , ,7.6e-6,
UIMP,1,REFT, , , ,
UIMP,1,NUXY, , ,0.28,
UIMP,1,PRXY, , , ,
UIMP,1,GXY, , , ,
UIMP,1,DAMP, , , ,
UIMP,2,EX, , ,110000,
UIMP,2,DENS, , , ,
UIMP,2,ALPX, , ,7.4e-6,
UIMP,2,REFT, , , ,
UIMP,2,NUXY, , ,0.26,
UIMP,2,PRXY, , , ,
UIMP,2,GXY, , , ,
UIMP,2,DAMP, , , ,
LESIZE,ALL, , ,10,1,1
FLST,2,3,4,ORDE,3
FITEM,2,14
FITEM,2,-15
FITEM,2,17
LESIZE,P51X, , ,20,1,
FLST,2,4,4,ORDE,4
FITEM,2,9
FITEM,2,11
FITEM,2,16
FITEM,2,20
LESIZE,P51X, , ,10,4,
FLST,2,1,4,ORDE,1
FITEM,2,9
LESIZE,P51X, , ,10,0.25,
FLST,5,4,5,ORDE,2
FITEM,5,3
FITEM,5,-6
CM,_Y,AREA
ASEL, , , ,P51X
CM,_Y1,AREA
CHKMSH,'AREA'
CMSEL,S,_Y
ESHAPE,2,0
AMESH,_Y1
```

```
ESHAPE,0,0
CMDEL,_Y
CMDEL,_Y1
CMDEL,_Y2
CM,matrix-e,ELEM
CM,matrix-n,NODE
CMGRP,matrix,MATRIX-A,MATRIX-E,MATRIX-K,MATRIX-L,MATRIX-N
VSEL,ALL
ASEL,ALL
LSEL,ALL
KSEL,ALL
ESEL,ALL
NSEL,ALL
CMSEL,U,MATRIX
TYPE,1,
MAT,2,
REAL,1,
ESYS,0,
FLST,5,2,5,ORDE,2
FITEM,5,1
FITEM,5,-2
CM,_Y,AREA
ASEL, , , ,P51X
CM,_Y1,AREA
CHKMSH,'AREA'
CMSEL,S,_Y
AMESH,_Y1
ESHAPE,2,0
ESHAPE,0,0
CMDEL,_Y
CMDEL,_Y1
CMDEL,_Y2
CM,cryst-n,NODE
CM,cryst-e,ELEM
CMGRP,crystal,CRYST-A,CRYST-E,CRYST-K,CRYST-L,CRYST-N
VSEL,ALL
ASEL,ALL
LSEL,ALL
KSEL,ALL
ESEL,ALL
NSEL,ALL
FLST,4,42,1,ORDE,4
FITEM,4,1
```

```
FITEM,4,-21
FITEM,4,1922
FITEM,4,-1942
CP,1,UY,P51X
FLST,4,82,1,ORDE,9
FITEM,4,982
FITEM,4,1002
FITEM,4,-1041
FITEM,4,1602
FITEM,4,-1621
FITEM,4,1922
FITEM,4,1963
FITEM,4,1983
FITEM,4,-2001
CP,2,UX,P51X
FLST,5,4,1,ORDE,4
FITEM,5,2
FITEM,5,1002
FITEM,5,1923
FITEM,5,1963
NSEL,U, , ,P51X
CPINTF,ALL,1e-6,
VSEL,ALL
ASEL,ALL
LSEL,ALL
KSEL,ALL
ESEL,ALL
NSEL,ALL
FLST,5,2,1,ORDE,2
FITEM,5,2
FITEM,5,1923
NSEL,S, , ,P51X
CPINTF,UX,1e-06,
VSEL,ALL
ASEL,ALL
LSEL,ALL
KSEL,ALL
ESEL,ALL
NSEL,ALL
FLST,5,2,1,ORDE,2
FITEM,5,1002
FITEM,5,1963
NSEL,S, , ,P51X
```

```
CPINTF,UY,1e-06,
VSEL,ALL
ASEL,ALL
LSEL,ALL
KSEL,ALL
ESEL,ALL
NSEL,ALL
FINISH
/SOLU
TUNIF,577,
TREF,577,
FLST,2,82,1,ORDE,10
FITEM,2,1
FITEM,2,42
FITEM,2,62
FITEM,2,-80
FITEM,2,342
FITEM,2,-381
FITEM,2,2263
FITEM,2,2304
FITEM,2,2324
FITEM,2,-2342
D,P51X, ,0, , , ,UX
FLST,2,42,1,ORDE,6
FITEM,2,1602
FITEM,2,1622
FITEM,2,-1641
FITEM,2,2284
FITEM,2,2304
FITEM,2,-2323
D,P51X, ,0, , , ,UY
```

APPENDIX B
TABULATED DATA

Table B.1. Data from BAS glass and glass-ceramic four-point flexural specimens.

ID#	Grow Time (h)	Height 1 (mm)	2 (mm)	3 (mm)	Width 1 (mm)	2 (mm)	3 (mm)	Indent Load (N)	Fail Load (kgf)	Width (µm)	Flaw Depth (µm)	Trace (µm)
3366901	0	6.015	6.030	6.030	3.390	3.390	3.375	9.8	201	205	77	232
3366902	0	6.030	6.015	6.015	3.450	3.425	3.425	9.8	173	213	90	238
3366903	0	6.005	6.015	6.030	3.400	3.425	3.375	9.8	189	211	85	233
3366904	0	6.005	5.990	5.990	3.375	3.400	3.400	9.8	169	138	45	211
3366905	0	5.980	5.980	5.965	3.400	3.425	3.475	4.9	266	134	53	130
3366906	0	6.015	6.015	6.015	3.400	3.425	3.475	4.9	255	134	51	149
3366908	0	6.045	6.045	6.030	3.400	3.310	3.310	4.9	254	158	74	153
3367301	0.5	6.055	6.055	6.055	3.260	3.340	3.365	9.8	268	117	51	153
3367302	0.5	6.055	6.055	6.055	3.375	3.365	3.350	9.8	229	198	63	189
3367303	0.5	6.030	6.030	6.030	3.375	3.390	3.400	9.8	262	198	68	175
3367304	0.5	6.045	6.045	6.045	3.325	3.350	3.350	4.9	357	121	48	119
3367305	0.5	6.015	6.015	6.015	3.375	3.365	3.325	4.9	375	106	37	81
3367306	0.5	6.030	6.030	6.030	3.350	3.350	3.050	4.9	330	117	44	199
3367307	0.5	5.990	5.990	5.965	3.340	3.340	3.145	9.8	293	129	55	139
3367308	32	5.965	5.965	5.965	3.175	3.175	3.145	9.8	395	134	66	161
3367311	32	5.965	5.965	5.990	3.350	3.375	3.400	9.8	424	155	58	127
3367312	256	5.990	6.005	5.990	3.350	3.375	3.425	4.9	436	152	66	143
3367313	256	5.965	5.965	5.965	3.325	3.325	3.285	4.9	405	156	66	146
3367315	256	5.940	5.940	5.940	3.300	3.325	3.250	9.8	270	156	61	157
3367326	4	6.015	6.015	6.030	3.100	3.125	3.340	9.8	333	137	58	188
3367327	4	6.015	6.015	6.015	3.225	3.225	3.275	9.8	335	137	57	157
3367328	4	6.030	6.030	6.015	3.275	3.275	3.325	4.9	312	153	64	153
3367331	4	6.015	6.015	6.015	3.200	3.325	3.325	9.8	153	153	68	185
3367332	4	6.015	6.015	6.015	3.300	3.300	3.325	9.8	259	178	68	149
3367333	4	5.965	5.965	5.965	3.365	3.350	3.340	4.9	334	128	45	165

Table B.2. Data for calculating the hardness of BAS glass and glass-ceramics.

ID#	Grow Time (h)	Diagonal Length 1 (μm)	2 (μm)	ID#	Grow Time (h)	Diagonal Length 1 (μm)	2 (μm)
3366901	0	38.2	40.0	3367311	32	39.7	41.5
3366901	0	40.0	39.7	3367311	32	41.8	43.8
3366901	0	42.7	42.0	3367312	32	40.9	42.7
3366905	0	41.2	39.1	3367312	32	41.5	41.2
3366905	0	41.5	40.3	3367312	32	40.0	40.3
3366905	0	37.9	38.8	3367312	32	41.8	41.8
3366905	0	38.8	38.8	3367317	256	45.3	45.3
3366905	0	39.7	40.3	3367317	256	44.4	41.8
3366906	0	40.3	40.9	3367317	256	42.9	42.4
3366906	0	39.1	39.1	3367318	256	40.8	48.6
3366906	0	37.6	39.1	3367318	256	50.0	46.8
3366906	0	39.7	39.7	3367318	256	42.1	38.5
3366907	0	39.7	40.6	3367318	256	42.9	42.9
3366907	0	39.1	38.8	3367319	256	43.8	43.8
3366907	0	38.2	39.1	3367319	256	43.8	44.7
3365507		23.1	41.8	3367321	256	42.1	41.8
3367301	0.5	37.	39.1	3367321	256	43.5	52.1
3367301	0.5			3367321	256	46.8	43.8
3367301	0.5	38.5	37.6	3367322	256	43.8	42.0
3367301	0.5	37.9	38.8	3367322	256	44.1	41.5
3367302	0.5	36.4	36.1	3367322	256	43.2	44.4
3367302	0.5	26.1	37.	3367322	256	40.6	42.1
3367302	0.5	38.2	40.3	3367325	4	37.9	37.3
3367302	0.5	32.7	39.1	3367325	4	40.0	37.9
3367304	0.5	36.1	39.4	3367325	4	39.4	39.7
3367304	0.5	37.0	38.2	3367325	4	39.4	39.7
3367304	0.5	37.3	39.7	3367326	4	38.5	39.4
3367304	0.5	37.8	42.0	3367326	4	40.9	40.9
3367309	32	38.5	37.6	3367326	4	40.0	40.3
3367309	32			3367326	4	38.2	40.3
3367309	32	39.4	39.4	3367327	4	38.5	38.5
3367309	32	40.9	39.7	3367327	4	36.7	38.5
3367310	32	39.7	40.3	3367327	4	38.2	36.7
3367310	32	38.8	39.7	3367327	4	37.0	37.3
3367310	32	38.5	44.1	3367328	4	39.4	40.9
3367311	32	39.4	42.1	3367328	4	40.4	40.0
3367311	32	41.5	41.5	3367328	4	40.6	42.9

Table B.3. Data for calculating the elasticity of BAS glass and glass-ceramics.

ID#	Growth Time (h)	Mass (g)	Volume (cm³)	Thickness (mm)	Time of Flight Longitude (ηs)	Shear (ηs)
3366901	0	1.615	0.5142	3.565	594	999
3366902	0			3.540	590	1030
3366903	0			3.540	590	1009
3366904	0			3.580	600	1059
3366905	0			3.515	582	1019
3366906	0			3.565	592	1049
3366907	0			3.540	590	1011
3366908	0			3.540	590	1030
3367301	0.5	1.597	0.5077	3.515	556	973
3367302	0.5			3.540	594	1063
3367303	0.5			3.565	580	1023
3367304	0.5			3.560	590	1049
3367305	0.5			3.475	560	998
3367306	0.5			3.515	560	989
3367307	0.5			3.590	590	1043
3367308	0.5	1.574	0.498	3.535	560	1013
3367309	32			3.535	560	959
3367310	32			3.50	570	1005
3367311	32			3.515	550	969
3367312	32			3.490	553	959
3367313	32			3.465	541	969
3367314	32			3.515	560	975
3367315	32			3.490	550	969
3367316	32			3.49	541	987
3367317	256	1.500	0.4719	3.325	490	863
3367318	256			3.325	469	858
3367319	256			3.185	460	850
3367320	256			3.325	471	870
3367321	256			3.325	480	918
3367322	256			3.110	454	860
3367323	256			3.390	490	899
3367324	256			3.175	460	849
3367325	4	1.525	0.4787	3.325	490	899
3367326	4			3.275	168	869
3367327	4			3.235	482	909
3367328	4			3.325	153	923
3367329	4			3.365	499	942
3367330	4			3.300	487	929
3367331	4			3.340	490	930
3367332	4			3.240	503	930

Table B.4. Dimensions of cross-sections between BAS crystals and stereological fields in the BAS glass-ceramic produced by crystal growth at 975°C for 0.5 h.

Major Axis (μm)	Minor Axis (μm)	Major Axis (μm)	Minor Axis (μm)	Major Axis (μm)	Minor Axis (μm)	Major Axis (μm)	Minor Axis (μm)
0.11	0.09	0.20	0.09	0.10	0.07	0.16	0.05
0.25	0.09	0.15	0.10	0.16	0.08	0.16	0.05
0.54	0.24	0.09	0.05	0.22	0.15	0.14	0.10
0.10	0.05	0.42	0.09	0.07	0.04	0.43	0.10
0.19	0.13	0.08	0.06	0.13	0.06	0.10	0.07
0.18	0.06	0.08	0.05	0.14	0.05	0.09	0.07
0.13	0.06	0.27	0.19	0.16	0.06	0.09	0.05
0.18	0.07	0.37	0.13	0.09	0.06		

Table B.5. Dimensions of cross-sections between BAS crystals and stereological fields in the BAS glass-ceramic produced by crystal growth at 975°C for 4 h.

Major Axis (µm)	Minor Axis (µm)	Major Axis (µm)	Minor Axis (µm)	Major Axis (µm)	Minor Axis (µm)	Major Axis (µm)	Minor Axis (µm)
0.39	0.26	0.52	0.06	0.21	0.09	0.43	0.26
0.23	0.18	0.18	0.13	0.47	0.35	0.21	0.09
0.69	0.33	0.15	0.10	0.80	0.35	0.39	0.20
0.35	0.16	0.12	0.14	0.80	0.29	0.52	0.20
0.42	0.22	0.30	0.20	0.32	0.15	0.38	0.16
0.20	0.09	0.27	0.07	0.65	0.42	0.82	0.27
0.30	0.15	0.38	0.12	0.27	0.27	0.12	0.10
0.20	0.18	0.28	0.25	0.18	0.14	0.26	0.21
0.15	0.10	0.79	0.63	0.60	0.34	0.19	0.09
0.26	0.15	0.60	0.15	1.06	0.43	0.24	0.20
0.17	0.16	0.86	0.23	0.47	0.39	0.20	0.14
0.18	0.17	0.74	0.25	0.33	0.20	0.17	0.14
0.19	0.19	0.69	0.27	0.28	0.20	0.46	0.29
0.11	0.09	0.41	0.30	0.51	0.15	0.59	0.27
0.14	0.10	0.16	0.14	0.44	0.23	0.82	0.49
0.13	0.10	0.29	0.23	0.24	0.18	0.27	0.24
0.39	0.37	0.24	0.22	0.27	0.20	0.38	0.21
0.39	0.21	0.23	0.10	0.24	0.14	0.44	0.36
0.31	0.06	0.25	0.06	0.27	0.19	0.31	0.25
0.37	0.15	0.26	0.08	0.40	0.30	0.67	0.39
0.22	0.21	0.29	0.21	0.49	0.19	1.18	0.29
0.29	0.11	0.24	0.14	0.58	0.28	0.55	0.44
0.28	0.07	0.14	0.14	0.36	0.32	0.50	0.28
0.45	0.30	0.19	0.11	0.66	0.29	0.22	0.19
0.82	0.45	0.66	0.47	0.59	0.21	0.32	0.22
0.15	0.14	0.34	0.25	0.50	0.27	0.69	0.47
0.14	0.27	0.41	0.11	0.37	0.14	0.15	0.20
0.24	0.15	0.62	0.23	0.26	0.26	0.17	0.14
0.35	0.26	0.14	0.09	1.26	0.75		
0.22	0.16			0.22	0.16		

108

Table B.6. Dimensions of cross-sections between BAS crystals and stereological fields in the BAS glass-ceramic produced by crystal growth at 975°C for 32 h.

Major Axis (μm)	Minor Axis (μm)	Major Axis (μm)	Minor Axis (μm)	Major Axis (μm)	Minor Axis (μm)	Major Axis (μm)	Minor Axis (μm)
0.86	0.58	2.86	0.58	1.19	0.36	0.86	0.53
0.65	0.42	0.49	0.34	0.22	0.18	0.69	0.60
0.81	0.41	1.55	0.91	0.23	0.21	0.96	0.43
0.42	0.41	0.62	0.35	0.19	0.16	0.81	0.56
0.55	0.38	0.61	0.34	0.27	0.27	0.61	0.38
0.41	0.37	0.41	0.32	0.62	0.21	1.25	0.38
0.55	0.36	0.63	0.34	0.44	0.27	1.03	0.44
0.57	0.49	0.66	0.46	0.79	0.51	0.88	0.37
0.44	0.35	0.27	0.14	0.56	0.29	0.62	0.27
0.66	0.63	0.36	0.23	1.00	0.91	0.69	0.51

Table B.7. Dimensions of cross-sections between BAS crystals and stereological fields in the BAS glass-ceramic produced by crystal growth at 975°C for 256 h.

Major Axis (μm)	Minor Axis (μm)	Major Axis (μm)	Minor Axis (μm)	Major Axis (μm)	Minor Axis (μm)	Major Axis (μm)	Minor Axis (μm)
1.31	0.67	2.06	0.58	1.84	1.61	0.65	0.16
0.67	0.56	2.08	0.96	1.64	1.47	0.92	0.28
0.57	0.43	3.34	1.39	1.25	0.79	0.38	0.16
1.01	0.53	2.27	1.63	1.29	0.97	0.54	0.24
1.45	0.82	0.91	0.46	4.83	4.54	1.39	0.46
1.09	0.65	0.53	0.38	1.38	1.08	2.33	0.58
1.81	0.45	3.12	1.04	1.41	1.44	3.70	2.99
1.28	0.74	1.90	1.79	1.07	0.65	0.80	0.41
0.88	0.45	0.82	0.73	0.61	0.99	0.64	0.44
0.73	0.38	4.15	1.94	1.42	1.06	0.52	0.26
2.39	1.63	1.21	1.17	0.69	0.59	0.84	0.44
0.93	0.67	5.62	0.60	0.68	0.24	0.74	0.50
1.50	0.40	1.32	0.27	0.57	0.97	1.16	0.31
0.70	0.40	1.37	0.41	1.44	0.91		
1.38	0.38	0.55	0.51	0.29	0.24		
0.50	0.45	0.90	0.35	0.52	0.22		

Table B.8. Data for calculation of the crystalline volume fraction and mean free path of the BAS glass-ceramic produced by crystal growth at 975°C for 0.5 h.

Points On Mica Per 25 Points	Intersections With αβ Interfaces Per 3.614 µm
16.5	79
20.5	73
17.5	70
20	69
18	78
19	79
18.5	78
18.5	78

Points On Mica Per 25 Points	Intersections With αβ Interfaces Per 3.614 µm
17.5	80
17.5	74
22	83
19	73
19	74
20.5	76
24	75
20.5	76

Table B.9. Data for calculation of the crystalline volume fraction and mean free path of the BAS glass-ceramic produced by crystal growth at 975°C for 4 h.

Points On Mica Per 25 Points	Intersections With αβ Interfaces Per 18.07 µm
16.5	16
24	29
16.5	32
20	28
18.5	18
19	17
16.5	19
18.5	29

Points On Mica Per 25 Points	Intersections With αβ Interfaces Per 18.07 µm
16	17
21	36
17.5	32
25	34
19	22
18	20
18	26
20.5	32

Table B.10. Data for calculation of the crystalline volume fraction and mean free path of the BAS glass-ceramic produced by crystal growth at 975°C for 32 h.

Points On Mica Per 25 Points	Intersections With αβ Interfaces Per 18.07 μm
17	13
14.5	13
17.5	22
17.5	20
11	18
17	15
19	13
22.5	10

Points On Mica Per 25 Points	Intersections With αβ Interfaces Per 18.07 μm
22.5	12
17.5	12
21	19
19	13
20	16
20.5	11
24	11
20	21

Table B.11. Data for calculation of the crystalline volume fraction and mean free path of the BAS glass-ceramic produced by crystal growth at 975°C for 256 h.

Points On Mica Per 25 Points	Intersections With αβ Interfaces Per 18.07 μm
18.5	18
20.5	10
20	18
18.5	10
18	12.5
20.5	4
19.5	9.5

Points On Mica Per 25 Points	Intersections With αβ Interfaces Per 18.07 μm
18.5	11.5
18.5	11.5
16.5	10
22	14
21	7
20.5	21
20.5	13
16	8.5

REFERENCES

Bansal NP, Hyatt MJ, Drummond CH, III (1991). Crystallization and properties of Sr-Ba aluminosilicate glass-ceramic matrices. *Ceram Eng Sci Proc* 12:1222-1234.

Bertolotti RL, Fulrath MF (1967). Effect of micromechanical stress concentrations on strength of porous glass. *J Am Ceram Soc* 50:558-562.

Binns DB (1962). Some physical properties of two-phase crystal-glass solids. In: Science of Ceramics. Stewart GH, editor. New York: Academic Press, pp. 315-334.

Borom MP (1977). Dispersion-strengthened glass matrices--Glass-ceramics, a case in point. *J Am Ceram Soc* 60:17-21.

Borom MP, Turkalo AM, Doremus RH (1975). Strength and microstructure in lithium disilicate glass-ceramics. *J Am Ceram Soc* 58:385-391.

Budiansky B, Amazigo JC, Evans AG (1988). Small-scale crack bridging and the fracture toughness of particulate-reinforced ceramics. *J Mech Phys Solids* 36:167-187.

Chan JY (1996). Mechanical Degradation of Canasite Glass-Ceramic Under Dynamic and Cyclic Fatigue (dissertation). Gainesville, FL: University of Florida.

Chantikul P, Anstis GR, Lawn BR, Marshall DB (1981). A critical evaluation of indentation techniques for measuring fracture toughness: II, strength method. *J Am Ceram Soc* 64:539-543.

Chyung CK, Beall GH, Grossman DG (1972). Microstructures & mechanical properties of mica glass-ceramics. In: Electron Microscopy and Structure of Materials. Thomas G, editor. Berkeley: University of California Press, pp. 1167-1194.

Cook RF, Lawn BR (1983). A modified indentation toughness technique. *J Am Ceram Soc* 66:C200-C201.

Davidge RW, Green TJ (1968). The strength of two-phase ceramic/glass materials. *J Mater Sci* 3:629-634.

112

Drummond CH, III, Bansal NP (1990). Crystallization behavior and properties of BaO·Al₂O₃·2SiO₂ glass matrices. *Ceram Eng Sci Proc* 11:1072-1086.

Evans AG (1972). The strength of brittle materials containing second phase dispersions. *Phil Mag* 26:1327-1344.

Evans AG (1976). On the formation of a crack tip microcrack zone. *Scripta Metall* 10:93-97.

Evans AG (1978). Microfracture from thermal expansion anisotropy--I. single phase systems. *Acta Metall* 26:1845-1853.

Evans AG, Faber KT (1981). Toughening of ceramics by circumferential microcracking. *J Am Ceram Soc* 59:371-372.

Evans AG, Faber KT (1984). Crack-growth resistance of microcracking brittle materials. *J Am Ceram Soc* 67:255-260.

Evans AG, Linzer M, Russell LR (1974). Acoustic emission and crack propagation in polycrystalline alumina. *Mater Sci Eng* 15:253-261.

Evans AG, McMeeking RM (1986). On the toughening of ceramics by strong reinforcements. *Acta Metall* 34:2435-2441.

Faber KT, Evans AG (1983a). Crack deflection processes--I. theory. *Acta Metall* 31:565-576.

Faber KT, Evans AG (1983b). Crack deflection processes--II. experiment. *Acta Metall* 31:577-584.

Frey WJ, Mackenzie JD (1967). Mechanical properties of selected glass-crystal composites. *J Mater Sci* 2:124-130.

Fullman RL (1953). Measurement of particle sizes in opaque bodies. *AIME Trans* 197:447-452.

Green DJ (1981). Stress-induced microcracking at second-phase inclusions. *J Am Ceram Soc* 64:138-141.

Green DJ, Nicholson PS, Embury JD (1979). Fracture of a brittle particulate composite. *J Mater Sci* 14:1657-1661.

Griffith AA (1920). The phenomena of rupture and flow in solids. *Phil Trans Roy Soc* 221A:163-198.

Griggs JA and Anusavice KJ (1997). Influence of thermal processing on crystallization rate in baria-fluormica glass-ceramic. In: Transactions of the Third International Congress on Dental Materials. Nakajima H and Tani Y, editors. November 4-8, 1997, Waikiki, Hawaii.

Hasselman DPH, Fulrath RM (1966). Proposed fracture theory of a dispersion-strengthened glass matrix. *J Am Ceram Soc* 40:68-72.

Hill TJ (1998). Effect of Crystal Morphology on Fracture and Fractal Dimension of Baria-Silicate Glass-Ceramic (thesis). Gainesville, FL: University of Florida.

Hilliard JE (1968). Measurement of volume in volume. In: Quantitative Microscopy. Rhines FN, DeHoff RT, editors. New York: McGraw-Hill, Inc., pp. 45-77.

Hing P, McMillan PW (1973). The strength and fracture properties of glass-ceramics. *J Mater Sci* 8:1041-1048.

Hoagland RG, Embury JD (1980). A treatment of inelastic deformation around a crack tip due to microcracking. *J Am Ceram Soc* 63:404-410.

Hoagland RG, Embury JD, Green DJ (1975). On the density of microcracks formed during the fracture of ceramics. *Scripta Metall* 9:907-909.

Ito T (1956). α-Celsian. In: X-ray Studies on Polymorphism. Tokyo: Maruren Co. Ltd., pp. 19-29.

Jessen TL, Mecholsky JJ, Moore RH (1986). Fast and slow fracture in glass composites reinforced with Fe-Ni-Co alloy. *Am Ceram Soc Bull* 65:377-381.

Juma'a QA, Parker JM (1981). Crystal growth in fluoride opal glasses. In: Nucleation and Crystallization in Glasses. Simmons JH, Uhlmann DR, Beall GH, editors. Washington, DC: The American Ceramic Society, Inc., pp. 218-236.

Khaund AK, Krstic VD, Nicholson PS (1977). Influence of elastic and thermal mismatch on the local crack-driving force in brittle composites. *J Mater Sci* 12:2269-2273.

Knehans R, Steinbrech R (1982). Memory effect of crack resistance during slow crack growth in notched Al_2O_3 bend specimens. *J Mater Sci Lett* 1:327-329.
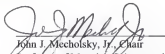
Lange FF (1970). The interaction of a crack front with a second-phase dispersion. *Phil Mag* 22:983-992.

Lange FF (1971). Fracture energy and strength behavior of a sodium borosilicate glass-Al₂O₃ composite system. *J Am Ceram Soc* 54:614-620.

Lin HC, Foster WR (1968). Studies in the system BaO-Al₂O₃-SiO₂ I. The polymorphism of celsian. *Amer Mineral* 53:134-144.

Marshall DB, Noma T, Evans AG (1983). A simple method for determining elastic-modulus-to-hardness ratios using Knoop indentation measurements. *J Am Ceram Soc* 65:C175-C176.

Mecholsky JJ, Freiman SW (1980). Effect of surface finish on the strength and fracture of glass. *J Non-Cryst Solids* 26:489-497.

Mecholsky JJ, Freiman SW, Rice RW (1977). Effect of grinding on flaw geometry and fracture of glass. *J Am Ceram Soc* 60:114-117.

Mecholsky JJ, Freiman SW, Rice RW (1978). Fractographic analysis of ceramics. In: Fractography in Failure Analysis, ASTM STP 645. Strauss BM, Cullen WH, editors. Philadelphia: American Society for Testing and Materials, pp. 363-379.

Nivas Y, Fulrath RM (1970). Limitation of Griffith flaws in glass-matrix composites. *J Am Ceram Soc* 53:188-191.

Pezzotti G (1993). On the actual contribution of crack deflection in toughening platelet-reinforced brittle-matrix composites. *Acta Metall Mater* 41:1825-1839.

Quinn GD, Gettings RJ, Kubler JJ (1994). Fracture toughness by the surface crack in flexure (SCF) method: Results of the VAMAS round robin. 15:846-855.

Rice RW, Freiman SW (1981). Grain-size dependence of fracture energy in ceramics: II, A model for noncubic materials. *J Am Ceram Soc* 64:350-354.

Sakai M (1991). Fracture mechanics and mechanisms of fiber-reinforced brittle matrix composites. *J Ceram Soc Japan* 99:983-992.

Sproull JF, Rindone GE (1973). Correlation between strength of glass and glassy microphases. *J Am Ceram Soc* 56:102-103.

Stett MA, Fulrath RM (1970). Mechanical properties and fracture behavior of chemically bonded composites. *J Am Ceram Soc* 53:5-13.

Swanson PL, Fairbanks CJ, Lawn BR, Mai Y-W, Hockey BJ (1987). Crack-interface grain bridging as a fracture resistance mechanism in ceramics: I, Experimental study on alumina. *J Am Ceram Soc* 70:279-289.

Swearengen JC, Beauchamp EK, Eagan RJ (1978). Fracture toughness of reinforced glasses. In: Fracture Mechanics of Ceramics. Bradt RC, Hasselman DPH, Lange FF, editors. New York: Plenum Press, pp. 973-987.

Talmy IG, Haught DA, Wuchina EJ (1992). Ceramics in the system $BaO \cdot Al_2O_3 \cdot 2SiO_2$ - $SrO \cdot Al_2O_3 \cdot 2SiO_2$ (BAS-SAS): Polymorphism, processing, and properties. *International SAMPE Electronics Conference* 6:687-698.

Uno T, Kasuga T, Nakajima K (1991). High-strength mica-containing glass-ceramics. *J Am Ceram Soc* 74:3139-3141.

Uno T, Kasuga T, Nakayama S, Ikushima AJ (1993). Microstructure of mica-based nanocomposite glass-ceramics. *J Am Ceram Soc* 76:539-541.

Zaykoski JA, Talmy IG (1994). Gallium and germanium substitutions in celsian. 15:779-786.

Zhou W, Zhang L, Yang J (1997). Preparation and properties of barium aluminosilicate glass-ceramics. *J Mater Sci* 32:4833-4836.
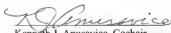
BIOGRAPHICAL SKETCH

Jason Alan Griggs was born in Rockledge, Florida, on June 24, 1970. He lived on the space coast of Florida, where his interest in engineering was supported by his parents and teachers, until the Fall of 1988, when he moved to Gainesville, Florida to begin collegiate studies at the University of Florida. He later received a Bachelor of Science degree from the Department of Materials Science and Engineering. Mr. Griggs entered the graduate program at the University of Florida in the Fall of 1993. On August 12, 1995, he married Amelia Rose Craig. They currently reside in Gainesville with their son, Alexander. Upon receiving his Doctor of Philosophy degree, Mr. Griggs will be employed as an Assistant Professor in the Department of Biomaterials Science at Baylor College of Dentistry.

I certify that I have read this study and that in my opinion it conforms to acceptable standards of scholarly presentation and is fully adequate, in scope and quality, as a dissertation for the degree of Doctor of Philosophy.

John J. Mecholsky, Jr., Chair
Professor of Materials Science and
Engineering

I certify that I have read this study and that in my opinion it conforms to acceptable standards of scholarly presentation and is fully adequate, in scope and quality, as a dissertation for the degree of Doctor of Philosophy.
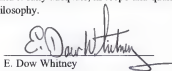
Kenneth J. Anusavice, Cochair
Professor of Materials Science and
Engineering

I certify that I have read this study and that in my opinion it conforms to acceptable standards of scholarly presentation and is fully adequate, in scope and quality, as a dissertation for the degree of Doctor of Philosophy.

Joseph H. Simmons
Professor of Materials Science and
Engineering

I certify that I have read this study and that in my opinion it conforms to acceptable standards of scholarly presentation and is fully adequate, in scope and quality, as a dissertation for the degree of Doctor of Philosophy.

E. Dow Whitney
Professor of Materials Science and
Engineering

I certify that I have read this study and that in my opinion it conforms to acceptable standards of scholarly presentation and is fully adequate, in scope and quality, as a dissertation for the degree of Doctor of Philosophy.

Mark C. Yang
Professor of Statistics

This dissertation was submitted to the Graduate Faculty of the College of Engineering and to the Graduate School and was accepted as partial fulfillment of the requirements for the degree of Doctor of Philosophy.

August, 1998

Winfred M. Phillips
Dean, College of Engineering

Karen A. Holbrook
Dean, Graduate School

LD
1780
1998
.G857